


Spring 4-22-2016

Understanding the Surface Induced Phosphorylation of Prebiotic Molecules by Schreibersite

Danna Qasim

Follow this and additional works at: http://digitalcommons.kennesaw.edu/mscs_etd

 Part of the [Geochemistry Commons](#), [Physical Chemistry Commons](#), and the [The Sun and the Solar System Commons](#)

Recommended Citation

Qasim, Danna, "Understanding the Surface Induced Phosphorylation of Prebiotic Molecules by Schreibersite" (2016). *Master of Science in Chemical Sciences Theses*. 8.
http://digitalcommons.kennesaw.edu/mscs_etd/8

This Thesis is brought to you for free and open access by the Department of Chemistry and Biochemistry at DigitalCommons@Kennesaw State University. It has been accepted for inclusion in Master of Science in Chemical Sciences Theses by an authorized administrator of DigitalCommons@Kennesaw State University. For more information, please contact digitalcommons@kennesaw.edu.

Understanding the Surface Induced Phosphorylation of Prebiotic Molecules by Schreibersite

by

Danna Qasim

Bachelor of Science Degree
Northern Arizona University, 2012

Submitted in Partial Fulfillment of the Requirements

For the Degree of Master of Science in the
Department of Chemistry and Biochemistry

Kennesaw State University

2016

Committee Chair

Graduate Program Coordinator

Committee Member

Department Chair

Committee Member

College Dean

ACKNOWLEDGEMENTS

Dr. Heather Abbott–Lyon for believing in me as a scientist.

Abbott–Lyon Laboratory group members for all their generous help.

Kennesaw State University, Department of Chemistry and Biochemistry for an excellent
Master’s program.

Center for Chemical Evolution for the supportive research environment.

Dr. Christopher Bennett for his scientific insights and friendship.

Dr. Stefanie Milam, Dr. Susanna Widicus Weaver and Dr. Cynthia Hartzell for their
support during a difficult time.

Alexandra Wolfarth for our long–time friendship.

Grandma Ana for watching over me during my residence in Atlanta.

Mom, Dad and Layla for always being there.

ABSTRACT

The study of the surface of a meteoritic mineral, schreibersite (Fe,Ni)₃P, was investigated to provide insight into the role of the mineral's surface in aqueous-phase phosphorylation reactions. The optimization of a custom-designed ultrahigh vacuum (UHV) apparatus and Fe₂NiP (schreibersite) surface was performed to permit surface science analysis. The bare surface was characterized by scanning electron microscopy (SEM) coupled with energy dispersive X-ray spectroscopy (EDS) and X-ray photoelectron spectroscopy (XPS), which showed some oxidation and segregation of phosphorous within the near-surface region. The interaction and/or reaction of water (H₂O), methanol (CH₃OH), formic acid (HCO₂H) and other molecules with the schreibersite surface at varying surface temperatures was probed by reflection absorption infrared spectroscopy (RAIRS) and temperature programmed desorption (TPD). At surface temperatures of approximately 130 K, H₂O interacts with Fe-P bridge sites while CH₃OH does not appear to interact with surficial phosphorus. The interaction between HCO₂H and surficial phosphorus is still under investigation. At 295 K, it is demonstrated that H₂O dissociatively chemisorbs as OH⁻ and lattice phosphorus undergoes oxidation. An increase in the surface temperature to about 500 K results in the recombinative desorption of OH⁻ as H₂O. Adsorption of other probe molecules such as H₂ and CO were not detected in the RAIRS experiments, and low dosages of pyridine (C₅H₅N) on the Fe₂NiP surface showed the presence of both Lewis and Brønsted acid sites.

TABLE OF CONTENTS

ACKNOWLEDGEMENTS.....	ii
ABSTRACT.....	iii
LIST OF TABLES/LIST OF FIGURES.....	vi
LIST OF KEY ACRONYMS.....	ix
CHAPTER 1. INTRODUCTION.....	1
1.1 Metal Phosphides: Applications, Synthesis and Analysis.....	1
1.2 Schreibersite: A Metal Phosphide Mineral as a Likely Prebiotic Catalyst.....	2
1.3 Influence of the Mineral Surface in Molecular Adsorption Behavior.....	5
1.4 Common Molecules on the early Earth.....	7
CHAPTER 2. EXPERIMENTAL METHODS.....	11
2.1 The Ultrahigh Vacuum Experimental Setup.....	11
2.2 Improvements to the Experimental Apparatus.....	13
2.3 Reflection Absorption Infrared Spectroscopy.....	18
2.3.1 Theory.....	18
2.3.2 Vibrational Frequencies and Line Shapes.....	22
2.4 Carbon Monoxide Adsorption Technique.....	23
2.5 Temperature Programmed Desorption.....	24
2.6 Scanning Electron Microscopy and Energy Dispersive X-ray Spectroscopy.....	26

2.7 X-ray Photoelectron Spectroscopy.....	28
2.8 Development of a Synthetic Schreibersite Sample and Iron-Nickel Control for Surface Science Analysis.....	30
CHAPTER 3: WATER AND HYDROGEN PEROXIDE ON SCHREIBERSITE	
3.1 RAIRS Data and Analysis of Water on Fe ₂ NiP and FeNi at Low Surface Temperatures (H ₂ O, H ₂ ¹⁸ O and D ₂ O).....	37
3.2 RAIRS Data and Analysis of Water on Fe ₂ NiP and FeNi at High Surface Temperatures (H ₂ O).....	48
3.3 TPD Data and Analysis of Water (D ₂ O and H ₂ O).....	50
3.4 RAIRS Data and Analysis of H ₂ O ₂	54
CHAPTER 4: SMALL ORGANICS ON SCHREIBERSITE	
4.1 RAIRS Data and Analysis of CH ₃ OH on FeNi and Fe ₂ NiP.....	55
4.2 RAIRS Data and Analysis of HCO ₂ H on FeNi and Fe ₂ NiP.....	60
4.3 RAIRS Data of Other Molecular Probes.....	63
CHAPTER 5: CONCLUSION.....	66
REFERENCES.....	68

LIST OF TABLES/ LIST OF FIGURES

FIGURE 1: Top view of fcc, bcc and hcp structures.....	5
FIGURE 2.1: Side view rendering of the experimental apparatus.....	12
FIGURE 2.2: Top view schematic of the experimental apparatus.....	13
FIGURE 2.3: Comparison of infrared background spectra.....	14
FIGURE 2.4: RAIRS of D ₂ O dosed on polished schreibersite before and after annealing the surface.....	15
FIGURE 2.5: RAIRS spectra of 4.0 L of H ₂ O dosed on Fe ₂ NiP with and without Ar ⁺ bombardment and flashing cycles.....	16
FIGURE 2.6: Images of the old and new sample holders.....	17
FIGURE 2.7: Drawing of the reflection geometry of the electric field components of infrared light.....	19
FIGURE 2.8: Schematic of the dipole moments of the vibrational modes of a molecule and the image dipole.....	21
FIGURE 2.9: Development of schreibersite sample for UHV analysis	31
FIGURE 2.10: Elemental maps of iron, nickel and phosphorus.....	31
FIGURE 2.11: Secondary electron images of the surface before and after flattening and polishing the schreibersite surface	32
FIGURE 2.12: SEM image of schreibersite surface after polishing with alumina suspension	34
TABLE 2.1: Atomic percent of elements within the sample taken by EDS.....	34
FIGURE 2.13: XPS of the unpolished Fe ₂ NiP sample.....	35

TABLE 2.2: Normalized data of the atomic percent of elements taken by XPS.....	35
FIGURE 3.1: Proposed adsorption geometry of H ₂ O on Fe ₂ NiP at a surface temperature of ~130 K.....	40
FIGURE 3.2: RAIRS spectra of H ₂ O adsorbed to Fe ₂ NiP at ~130 K.....	41
TABLE 3.1: Vibrational frequencies of H ₂ O adsorbed to Fe ₂ NiP at ~130 K.....	42
FIGURE 3.3: RAIRS spectra of H ₂ O adsorbed to FeNi control at ~140 K.....	43
FIGURE 3.4: RAIRS spectra of H ₂ ¹⁸ O control molecule adsorbed to Fe ₂ NiP at 135 K...	43
FIGURE 3.5: A RAIRS spectra of D ₂ O control molecule adsorbed to Fe ₂ NiP at ~120 K.....	44
FIGURE 3.6: RAIRS spectra of H ₂ O adsorbed to Fe ₂ NiP one day after Ar ⁺ bombardment and flashing cycles.....	45
FIGURE 3.7: RAIRS spectra of H ₂ O adsorbed to Fe ₂ NiP two days after Ar ⁺ bombardment and flashing cycles and one day after H ₂ O experiment.....	46
FIGURE 3.8: RAIRS spectra of H ₂ O adsorbed to Fe ₂ NiP two days after Ar ⁺ bombardment and flashing cycles and no experiments taken in between.....	47
FIGURE 3.9: RAIRS spectra of H ₂ O adsorbed to Fe ₂ NiP two days after Ar ⁺ bombardment and flashing cycles and no experiments taken in between and one day after H ₂ O experiment.....	48
FIGURE 3.10: RAIRS spectra of H ₂ O dosed onto variable temperature surfaces of Fe ₂ NiP and FeNi.....	50
FIGURE 3.11: TPD spectrum of 6.0 L of H ₂ O dosed onto Fe ₂ NiP.....	51
FIGURE 3.12: TPD spectrum of 6.0 L of H ₂ O dosed onto Fe ₂ NiP.....	52
FIGURE 3.13: TPD spectrum of 5.0 L of H ₂ O dosed onto Fe ₂ NiP.....	53
FIGURE 3.14: TPD spectrum of 5.0 L of D ₂ O dosed onto Fe ₂ NiP.....	53
FIGURE 3.15: RAIRS spectra of H ₂ O ₂ adsorbed to Fe ₂ NiP at ~130 K.....	54
FIGURE 4.1: RAIRS spectra of CH ₃ OH and CH ₃ OH dissociation products adsorbed to Fe ₂ NiP at 120 K.....	57
FIGURE 4.2: Drawing of the dissociation of CH ₃ OH as CH ₃ O ⁻ and H ⁺ on Fe ₂ NiP at 120 K.....	57

FIGURE 4.3: RAIRS spectra of CH ₃ OH adsorbed to FeNi at ~140 K.....	58
TABLE 4.1: Vibrational frequencies of CH ₃ OH adsorbed to Fe ₂ NiP at 120 K.....	59
FIGURE 4.4: Proposed adsorption geometry of HCO ₂ H on Fe ₂ NiP at a surface temperature of ~130 K.....	60
FIGURE 4.5: RAIRS spectra of HCO ₂ H adsorbed to Fe ₂ NiP at ~130 K.....	62
FIGURE 4.6: RAIRS spectra of HCO ₂ H adsorbed to FeNi at 136 K.....	62
TABLE 4.2: Vibrational frequencies of HCO ₂ H adsorbed to Fe ₂ NiP at ~130 K.....	63
FIGURE 4.7: RAIRS spectra of C ₅ H ₅ N adsorbed to Fe ₂ NiP at ~130 K.....	64
FIGURE 4.8: RAIRS spectra of CO adsorbed to Fe ₂ NiP at ~130 K.....	65
FIGURE 4.9: RAIRS spectra of H ₂ adsorbed to Fe ₂ NiP at 116 K.....	65

LIST OF KEY ACRONYMS

UHV: ultrahigh vacuum

SEM: scanning electron microscopy

EDS: energy dispersive X-ray spectroscopy

XPS: X-ray photoelectron spectroscopy

RAIRS: reflection absorption infrared spectroscopy

TPD: temperature programmed desorption

CHAPTER 1. INTRODUCTION

1.1 Metal Phosphides: Applications, Synthesis and Analysis

Metal phosphides have been prepared as nanoparticles and in bulk form for applications in technology and catalysis. Nanoparticles have been synthesized using phosphorous sources such as elemental phosphorous,^{1,2} $\text{P}(\text{SiMe}_3)_3$,^{1,2} tri-*n*-octylphosphine,^{1,2,3} alkyl- and arylphosphines,¹ PCl_3 ,^{1,2} and Na_3P .^{1,2,3,4} By changing the properties of the nanoparticles (e.g. size, shape, etc.), nanoparticles can be used to dictate the surface states of materials.^{1,2,5} The growth of single crystals and other bulk materials have been performed to investigate how the behavior of the material is influenced by the orientation of the surface as well as to develop new materials.^{1,6,7,8,9,10}

The analysis of metal phosphides has been carried out using a variety of tools. X-ray Absorption Near Edge Structure (XANES),^{1,11} Extended X-ray Absorption Fine Structure (EXAFS),^{1,12} Infrared Spectroscopy (IR),^{12,13} X-ray Photoelectron Spectroscopy (XPS)^{1,11,14} and Density Functional Theory (DFT)^{1,15} were utilized to probe oxidation states, behavior of active sites on the surface, surface composition and density of states. It was illustrated that Fe and Ni each have unique properties that were apparent by chemistry observed at the surface. Compared to the Ni–Ni distance, a study has shown that the Fe–Fe distance in Fe_2P is relatively large and allows for multiple molecules to adsorb to one site, although Ni is much more susceptible to interacting with CO than Fe

is.¹² The same study also demonstrated that the change in the Ni:Fe molar ratio in a NiFeP/SiO₂ catalyst affects the type of catalytic process that occurs. Particularly, Ni sites are active for hydrodesulfurization but Fe sites are not. It is interesting to note that although Fe and Ni behave differently, the oxidation state of phosphorus in M₂P and M₃P (M = metal) samples has been suggested to be the same and is approximately -1 .¹

Crystal structures have been evaluated by solid-state Nuclear Magnetic Resonance (NMR),^{1,16} X-ray Diffraction (XRD)^{1,14,17,18} and High-Resolution Transmission Electron Microscopy (HRTEM).^{1,18,19} As mentioned previously, the incorporation of Fe versus Ni into a sample results in unique outcomes. It has been shown that the particle size of Fe₂P is greater than the particle size of Ni₂P.¹⁷ The synthesis of Ni₂P microspheres has been performed by the reduction of NiO by PH₃.¹⁸ However, the synthesis of Fe₂P does not undergo the same procedure due to the nature of Fe versus Ni. In addition to Fe and Ni phosphides, it has been suggested that a surface of indium phosphide (InP) nanoparticles can be oxidized by H₂O to yield indium phosphate.¹ Limited studies have been performed with Scanning Electron Microscopy (SEM) to examine the morphology of metal phosphide samples, which have shown that InP nanowires can assemble into an intricate structure by applying an electric field.²⁰

1.2 Schreibersite: A Metal Phosphide Mineral as a Likely Prebiotic Catalyst

As mentioned, metal phosphides exhibit a myriad of interesting properties that have applications in technology and heterogeneous catalysis. Regarding technological applications, metal phosphides have been exploited in battery research,^{21,22} as magnetic refrigerants²³ and superconductors.²⁴ Their high catalytic activity in hydrotreating

processes such as hydrodesulfurization (HDS),^{16,25,26,27,28} hydrodenitrogenation (HDN),^{16,25,26,27,28} hydrodeoxygenation (HDO),^{28,29,30} and hydrodechlorination (HDCI),^{14,31,32,33} as well as their electrocatalytic activity in clean-energy science^{34,35,36,37} have made them impactful catalysts in today's industries.

Due to the promising applications that metal phosphides have brought to the heterogeneous catalysis community, it is not surprising that metal phosphide minerals are currently under speculation for catalyzing chemical reactions on the early Earth that may have contributed to the origin of life. One way to bridge metal phosphide mineral catalysis and the formation of basic biomolecules is to address the phosphorous problem that is prevalent in the origin of life research.

Phosphorous is a fundamental element in biochemistry and is commonly found as part of an orthophosphate group (i.e., PO_4^{3-}). Such groups are prevalent in the backbone of nucleic acids (such as RNA and DNA), energy transport molecules (such as ATP and ADP), and structure molecules (such as phospholipids).³⁸ These orthophosphate groups also have poor chemical reactivity and water solubility,³⁹ which is paradoxical since water is where most metabolic reactions take place. This raises the question "How did orthophosphate become prevalent in life systems?"

A number of recent studies have been performed on the meteoritic mineral, schreibersite ($\text{Fe,Ni}_3\text{P}$), as the mineral is proposed to be the ultimate source of phosphorus in life systems.^{40,41,42,43,44,45,46,47,48,49} Schreibersite has a tetragonal crystal system and is typically found in a matrix consisting of metallic iron minerals.⁵⁰ It has a range of compositions (e.g. Fe_3P , Fe_2NiP , Ni_3P , etc.) with the constraint that the

empirical formula contains a metal to phosphide ratio of 3 to 1. Because schreibersite is isomorphic,^{51,52} the space group will be the same regardless of the metal (iron or nickel) in the lattice, however, the unit cell dimensions will be different due to the difference in atomic size. It is very brittle, with a mineral hardness of 6.5–7 and a density of 7.0–7.3 g/cm³.⁵⁰ The phosphorous in schreibersite has an oxidation state between 0 and –1.^{42,53} In the Ni₃P form, the surface energy ranges from –7.1 eV (nickel rich termination) to –5.36 eV (phosphorous rich termination). It also has virtually no band gap at the Fermi level, making schreibersite a conductive mineral.¹⁵

Due to the estimates of the abundance of schreibersite-containing meteorites delivered to the Earth's surface during the late heavy bombardment,⁵⁴ it is plausible that schreibersite was a source of reactive phosphorous on the early Earth. It was also discovered that the reactive phosphorous species, phosphite, existed in the early Archean ocean, which was likely a result of meteor impacts.⁴⁸ Schreibersite is known to phosphorylate biomolecules such as glycerol and choline,⁴⁹ and has been shown to react under anoxic atmospheres,⁴⁶ which mimic the reducing atmosphere that is believed to have existed during the period that life evolved on Earth.³⁹ These scenarios illustrate the likelihood of schreibersite as a prebiotic source of phosphorous. Further investigations on the formation pathways of phosphorus-containing molecules by schreibersite could aid in resolving the phosphorus issue.

Most of the recent studies on schreibersite analyze the corrosion and phosphorylation products in aqueous solution, yet there is little information on how these products are formed. Because these reactions occur in the presence of schreibersite, it is

hypothesized that the mineral surface has a role in product formation. In particular, phosphorylation of nucleosides such as adenosine and uracil has only been successfully performed in the presence of the mineral,⁴⁹ suggesting a surface-mediated process. By observing the chemical kinetics and reaction dynamics at the mineral interface, the conditions that govern the production of these phosphorus-containing species may be better understood.

1.3 Influence of the Mineral Surface in Molecular Adsorption Behavior

How mineral surfaces impact the chemistry at the interface is discussed in this section. Before examining the complex features of a mineral surface, it is helpful to review the formation of the simple idealized crystalline surface. A solid structure is typically viewed as consisting of two parts: the bulk structure and the near surface region called the selvedge.⁵⁵ By observing the bulk structure and how it intersects with the near surface region, the type of surface can be predicted. For a perfect metallic crystal, the most common structures are the face-centered cubic (fcc), body-centered cubic (bcc) and hexagonal close-packed (hcp) structures and are illustrated in Figure 1. The ideal surface has a two-dimensional periodic arrangement of atoms, and the bulk structure is a collection of replicating three-dimensional unit cells.

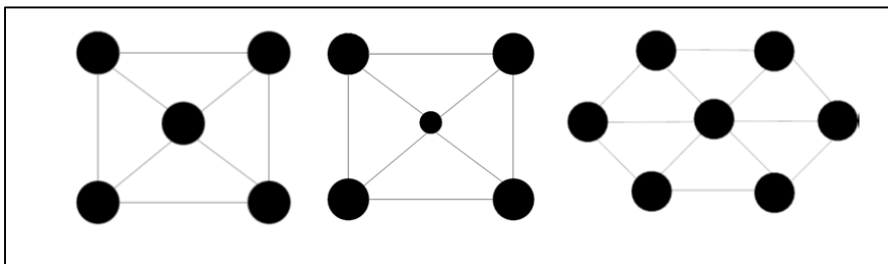


Figure 1. (to right) A top view of fcc, bcc and hcp structures.

Another way to describe an ideal surface is that it is essentially composed of replicating lattice planes. The orientation of these planes is indicated by the Miller indices.⁵⁵ Depending on the angle at which the crystal is cut, an infinite number of surfaces can be studied. Idealized (i.e., simple and flat) surfaces consist of the low-index planes (e.g. (100), (111), and (110)). These low-index planes provide sites for adsorbates to bond to due to the presence of unsaturated coordination upon cutting the crystal. Sites include one-fold coordination (terminal bonding), two-fold coordination (bridging), three-fold coordination (three-fold hollow), and other coordinations.⁵⁵ Although there is a large library of references that illustrate that flat surfaces can induce chemical reactions, it has been experimentally determined that defect sites (steps, kinks, terraces, etc.), which are features found on real crystal surfaces, drive some catalytic processes.^{55,56}

Mineral surfaces carry features of real crystal surfaces as well as additional intricacies.^{57,58,59} Most mineral surfaces are irregular (not periodic)⁵⁷ and contain a relatively high amount of defect sites, which can provide docking sites for adsorbates.^{59,60,61,62,63} To better understand how and why certain sites on mineral surfaces govern the chemistry that occurs on mineral surfaces, a background on the fundamental

principles that dictate the geometric and electronic structure of mineral surface atoms is essential.⁶⁴

There are three main principles that govern the structure of atoms on mineral surfaces.⁶⁴ The first principle is based on autocompensation of the surface. If the surface is autocompensated, then the material is said to have a neutral charge and is, therefore, stable. A surface that is not autocompensated will relax and even reconstruct, which can lead to a growth of defect sites on the surface.

The second principle is based on the rise in energy on the surface when dangling bonds rehybridize in order for the surface atoms to become more stable.⁶⁴ Rehybridization can occur by charge transfer between surface atoms, bond formation between surface atoms, or bond formation between surface atoms and adsorbates (i.e. adatoms). All these processes lead to a change in the properties of the surface.

The last principle that influences the geometric structure of surfaces is the conditions that the surface is exposed to.⁶⁴ Surface atoms want to stay thermodynamically stable, but the environmental conditions may force the surface atoms to maintain a thermodynamically less favorable structure. Therefore, the surface-processing conditions are significant in the formation of the surface geometry.

1.4 Common Molecules on the early Earth

The molecules chosen in this thesis to potentially react with the schreibersite surface are regarded as common molecules on the early Earth. Additionally, some of the listed molecules have been exploited in related experiments to probe different surface sites.

Water (H₂O), colloquially deemed the elixir of life, has been detected in all stages of matter in space, from jets emanating from stars,⁶⁵ molecular clouds in the interstellar medium⁶⁶ and protoplanetary disks far from our Solar System,⁶⁷ to nearby comets, asteroids and the terrestrial planets such as Earth, Mercury and Mars. Consequently, many of the solution-based schreibersite experiments occurred in an aqueous solvent, which is why H₂O was selected as an adsorbate for the surface science experiments presented in this work. The adsorption of H₂O on Fe and Ni terminated surfaces has been investigated in the literature^{68,69,70,71,72} and the experimental vibrational frequencies were used to aid in assignment of the bands found in the experiments presented in this thesis. (These references contained High Resolution Electron Energy Loss Spectroscopy (HREELS) data versus Reflection Absorption Infrared (RAIRS) data since HREELS experiments were more abundant in the literature. It is important to note that unlike RAIRS, HREELS is sensitive to many sources of vibrational excitation.⁷³ Yet RAIRS, unlike HREELS, has the ability to operate at a variety of pressures (i.e., not limited to UHV) and has much higher resolution (4 cm⁻¹) than is typically found in HREELS experiments.⁷³ For these reasons, RAIRS and HREELS are often used to complement one another). The majority of the referenced experiments show that H₂O forms clusters on iron and nickel surfaces at cold temperatures and breaks apart into hydroxyls at surface temperatures between 200 – 300 K. The dissociation of H₂O and subsequent formation of a hydroxylated surface can happen at cold surface temperatures, if the surface is covered with less than a monolayer of oxygen.⁷⁰

To help constrain the corrosion reaction mechanism, an oxidizing molecule, hydrogen peroxide (H₂O₂), was chosen as an adsorbate. H₂O₂ has also been generated by

pyrite (a mineral well-known in the origin of life community) reacting with H₂O under an anoxic environment,⁷⁴ which suggests H₂O₂ is potentially important in early Earth chemistry. An infrared study of H₂O₂ in a titanium silicate sieve⁷⁵ was used as a reference in this thesis. That work showed that the oxidizing agent, TiOOH, is formed and able to oxidize small hydrocarbon chains.

Methanol (CH₃OH) and formic acid (HCO₂H) are simple organic molecules and are prebiotically relevant,^{76,77} making them candidates for the analysis of plausible surface-induced phosphorylation chemistry. Moreover, they each contain an OH group, which is the typical functional group that is phosphorylated in biochemical systems. The adsorption of CH₃OH^{78,79,80,81,82} and HCO₂H^{79,83} on iron and nickel based surfaces has been studied and the vibrational signatures are used as references. Most of the experiments for CH₃OH adsorption suggest that CH₃OH dissociates into methoxy (CH₃O⁻) at low coverages and at low and high surface temperatures, whereas one experiment suggests that the missing OH vibrational frequency is due to a hydroxyl hydrogen interacting with a lattice oxygen.⁸⁴ HCO₂H adsorption studies illustrate that HCO₂H is able to physisorb via hydrogen bonding and dissociatively chemisorb as HCOO⁻ and CO at low and high surface temperatures.^{81,85}

Pyridine has been widely used to probe Lewis acid and Brønsted acid sites particularly because the vibrational frequencies have been characterized and the line profiles are well-resolved.⁸⁶ Vibrational studies of pyridine adsorption on iron and nickel terminated surfaces have been well investigated.^{87,88,89,90,91,92} It has been shown that Lewis acid sites dominate mesoporous-supported Ni₂P catalysts as well as goethite and

phosphated goethite,^{89,91} and that Brønsted acidity is predominately found in SiO₂-supported Ni₂P samples.⁸⁸ These findings help characterize the complex nature of the schreibersite surface.

This thesis describes the characterization of the Fe₂NiP surface as well as the interaction of H₂O, CH₃OH, HCO₂H and other small molecules with the Fe₂NiP surface. Chapter 2 is a review of the methods that are used to characterize the surface and probe surface reactions. Additionally, Chapter 2 contains details on the development of a metal phosphide mineral that is conducive to RAIRS and the design of a custom-built UHV apparatus that is dedicated to analyzing mineral surfaces. The focus in Chapter 3 is on the interaction of H₂O with Fe₂NiP and FeNi at various surface temperatures. Lastly, Chapter 4 contains a discussion primarily on the interaction of organics with Fe₂NiP and FeNi at low surface temperatures.

CHAPTER 2. EXPERIMENTAL METHODS

2.1 The Ultrahigh Vacuum Experimental Setup

The ultrahigh vacuum (UHV) chamber reaches a base pressure of $\sim 3.0 \times 10^{-10}$ torr and is designed to conduct surface science experiments. The chamber contains a turbomolecular pump (Pfeiffer TPU 170) backed by a rotary–vane mechanical pump (Oerlikon Leybold NT16), a rotary–vane mechanical pump connected to the gas manifold (Oerlikon Leybold NT5), two Convector gauges that read a minimum pressure of 1×10^{-4} torr (Granville–Phillips 275), an ionization gauge that reads a minimum pressure of 3×10^{-11} torr (Nude Bayard–Alpert Hot Cathode), a quadrupole mass spectrometer (Hiden HALO 201–RC), a Fourier transform infrared spectrometer (Nicolet 6700), and an electron gun with energies from 5–2000 eV (Kimball Physics ELG–2).

Solid and pressed/powder samples are attached to a sample manipulator that rotates via a differentially pumped rotational stage (McAllister DPRF 275), which is pumped by a rotary–vane mechanical pump (Edwards RV12 H.P.). Surface temperatures ranging from 100 to 680 K are achieved using liquid nitrogen cooling and by heating radiatively. A tantalum plate is spot–welded to the back of the sample to improve the cooling, and tungsten wires with a diameter of 0.01” are wrapped around the tantalum to radiatively heat the sample. Ices are deposited by dosing gases and vapors onto mineral samples via a variable leak valve attached to a gas manifold. Ice thicknesses are reported by dosage where 1 Langmuir (L) is equivalent to 1×10^{-6} torr*s of exposure to an

ambient gas. Assuming the molecular sticking coefficient is unity when the surface temperature is very low (< 135 K), a 1.0 L dose will result in one monolayer of adsorbed molecules on the surface.

Schematics of the experimental setup in the Abbott–Lyon Laboratory are shown in the Figures 2.1 and 2.2 below.

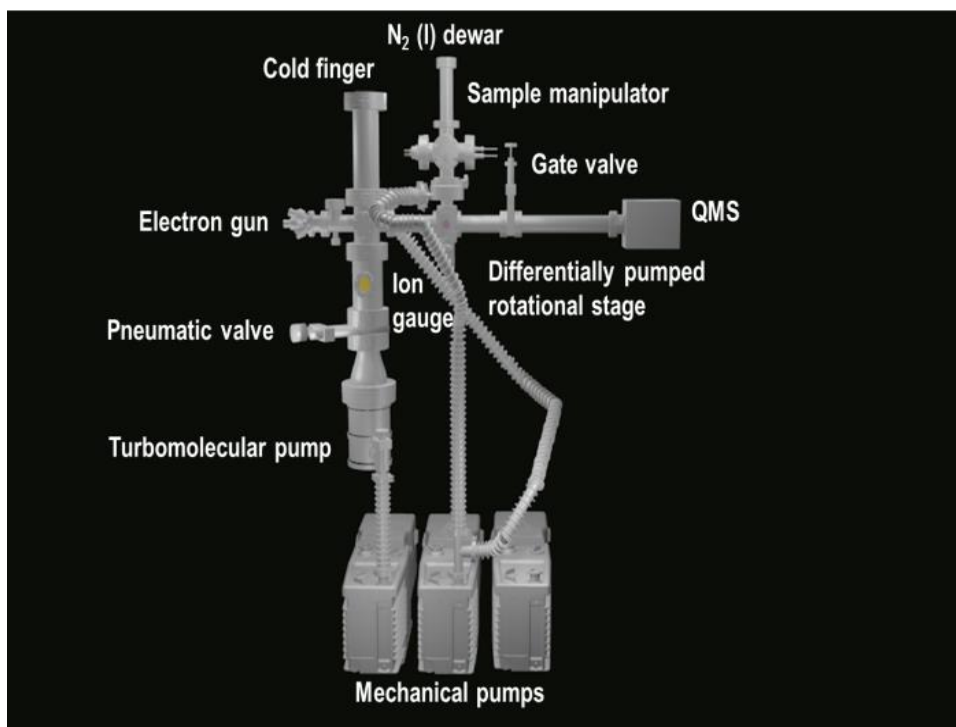


Figure 2.1 A side view rendering of the experimental apparatus used in this thesis. Drawing produced in the software Blender.

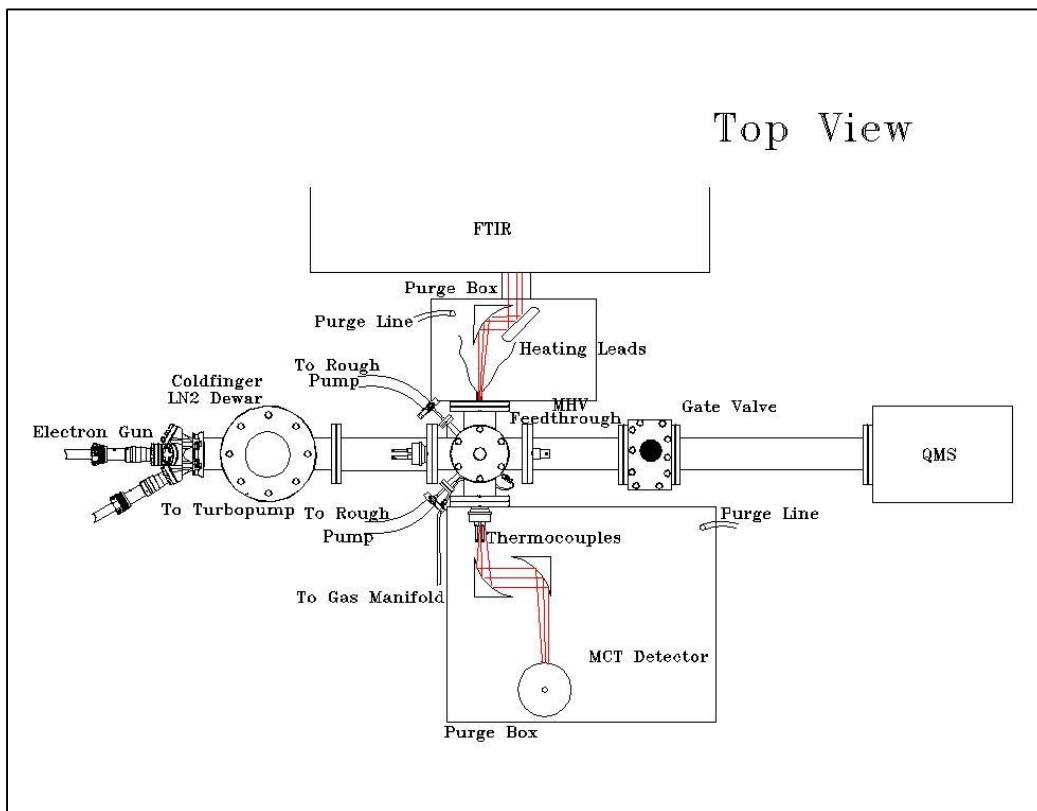


Figure 2.2 A top view schematic of the experimental apparatus used in this thesis. The red lines represent infrared light. Drawing produced in the software DraftSight.

2.2 Improvements to the Experimental Apparatus

A significant portion of this thesis study was dedicated to optimizing the experimental apparatus, in particular, to improve the RAIRS experiments. Therefore, these topics will be discussed. Bigger optical breadboards were installed so that the mirrors could be positioned around the chamber to aim the light at 80° to surface normal. To reduce gas-phase peaks in the infrared data, new purge boxes were designed and nitrogen gas replaced filtered compressed air as the purge gas in the FTIR. The resulting infrared background scan is presented in Figure 2.3. The time required to align the

infrared light for RAIRS experiments was greatly reduced (from days to minutes) by employment of a white light source and calcium fluoride beamsplitter.

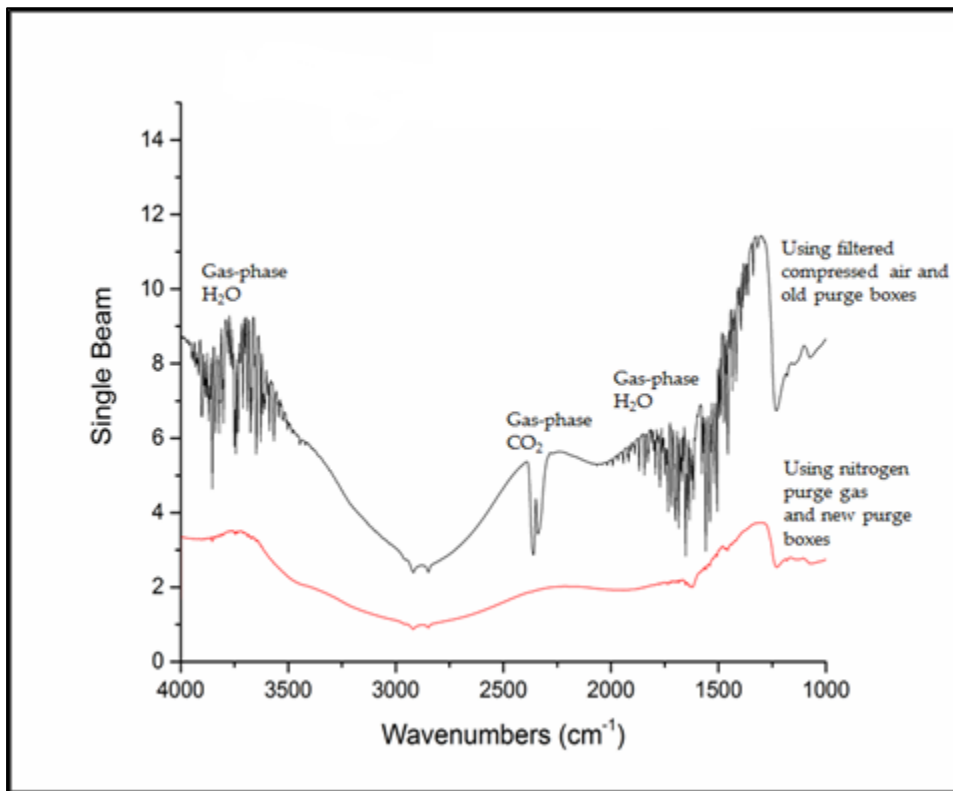


Figure 2.3 Comparison of Infrared background spectra. The red line is a background scan that represents the background when nitrogen gas is used to purge the FTIR. The black line is a background scan that represents the background when filtered compressed air is used to purge the FTIR.

Additionally, the range and control of the surface temperature was improved. A cartridge heater was replaced by resistive heating with tungsten wire and tantalum foil in order to reduce outgassing by the cartridge heater. A high temperature of 680 K was achieved through radiative heating, which was high enough to remove contaminants from the surface and subsequently lead to improved signal in the infrared data. Figure 2.4 shows that the infrared signal intensity for a 10.0 L dose of H₂O after annealing the

sample (Fig. 2.4a) is comparable to the signal intensity for a 100.0 L dose prior to annealing the sample to remove contaminants (Fig 2.4b).

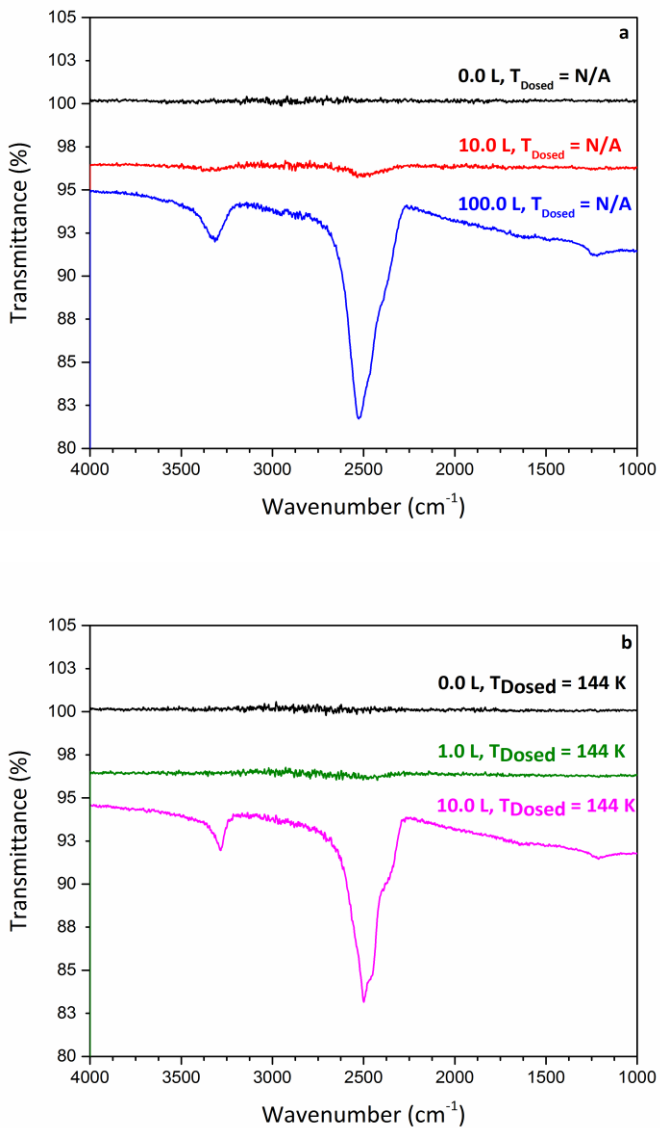


Figure 2.4 (a) RAIRS of D₂O dosed on polished schreibersite before annealing the surface and (b) after annealing the surface. The response of the system to 10.0 L of D₂O was improved by a factor of 10 as seen by comparison of the intensity of the peaks before and after annealing.

The removal of contaminants from the mineral surface was further enhanced by use of an argon ion (i.e., Ar^+) bombardment and flashing procedure. The procedure required three cycles of argon ion bombardment and flashing the day before an experiment. To bombard the sample with argon ions, the sample was negatively biased to 2000 V, 5×10^{-5} torr of argon was used to fill the chamber and an electron gun acted as the argon ionization source. After bombardment for thirty minutes, the sample was flashed to 550 K. Figure 2.5 shows that the described procedure was robust enough to remove the species represented by the 1220–1240 cm^{-1} peak.

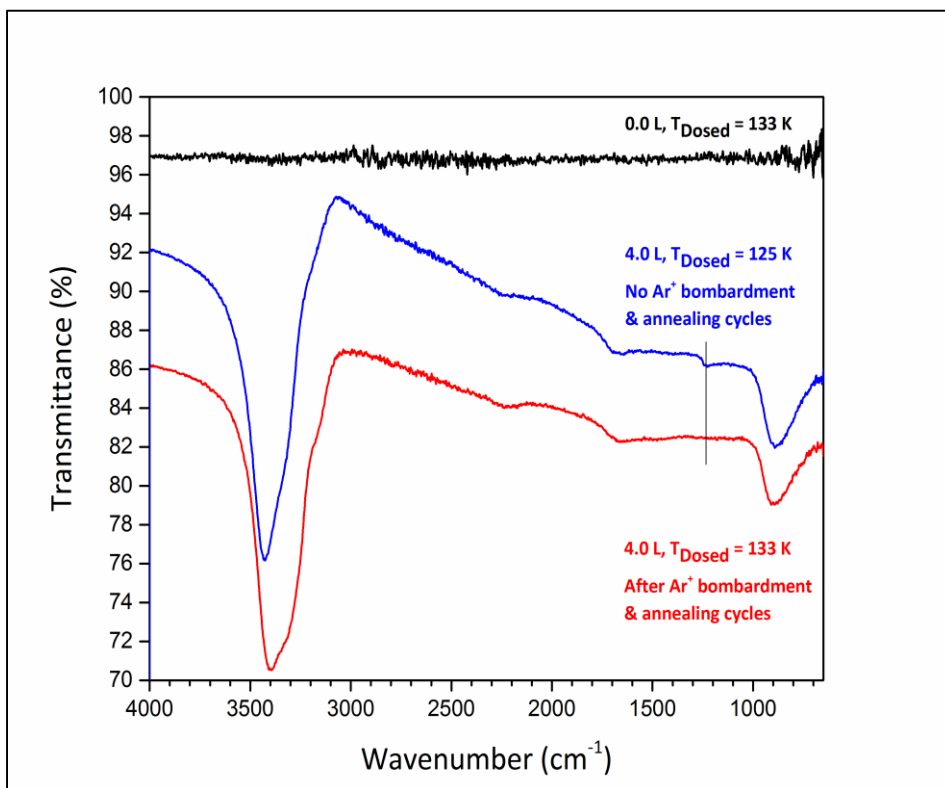


Figure 2.5 RAIRS spectra of 4.0 L of H_2O dosed on Fe_2NiP . The blue spectrum was taken without performing the argon ion bombardment and flashing procedure the day before the experiment, and the red spectrum was taken the day after performing the procedure.

Although the sample temperature was higher in the red spectrum experiment compared to the blue spectrum experiment, as shown in Figure 2.4b, the 1220–1240 cm^{-1} peak has been observed at temperatures above 133 K and, therefore, was not expected to vanish at 133 K.

Cooling of the sample was optimized by incorporation of a new sample holder, which was designed and constructed by T. Beckman from the Abbott–Lyon Laboratory. A comparison of the old and new sample holders are illustrated in Figure 2.6. The new sample holder improved the cooling by decreasing the number of junctions between separate pieces of copper. (Note that the new sample holder is machined from a single block of oxygen–free copper.) Additionally, having a single post positioned behind the sample made alignment for RAIRS easier and decreased the opportunity for desorption from the face of the posts during temperature programmed desorption (TPD) experiments.



Figure 2.6 (a) old sample holder and (b) new sample holder.

Finally, a new LabVIEW program was written by A. Pital and T. Beckman from the Abbott–Lyon Laboratory to accurately correlate the mass of up to four desorbing species to the desorption temperatures. A maximum linear ramp rate of 1 K/sec was achieved through A. Pital’s portion of the LabVIEW code. These improvements to the temperature control and monitoring were necessary for TPD experiments.

2.3 Reflection Absorption Infrared Spectroscopy

2.3.1 Theory

Reflection absorption infrared spectroscopy produces an infrared spectrum of the light reflected from the surface that illustrates the absorption peaks characteristic to the adsorbed molecule. The measurement of the vibrational frequency of the functional group gives direct information on the binding sites as well as the binding geometry of the adsorbate.^{93,94} In order to understand how this process works, an understanding of how light interacts with the adsorbate is necessary.

The infrared spectroscopy selection rule states that in order for a vibration to be infrared active, the energy of the infrared light must match the energy difference between two vibrational states, and the transition between the vibrational states induces a change in the dipole moment of the vibration. Mathematically, this is described as:⁹⁴

$$\text{Intensity} \propto |\psi_f^* E \mu_{fi} \psi_i|^2 \quad (1)$$

where E is the electric field vector and μ_{fi} is the transition dipole moment.

Optimization of a RAIRS signal requires additional considerations. The first consideration is that only the p–component of the infrared light interacts with the

adsorbed species. The infrared light that hits the surface can be described as an electromagnetic wave that has magnitude and direction and, therefore, is composed of electric field vectors. The electric field vectors can be further branched into two components: s-component (s-polarized) and p-component (p-polarized). The s-component is orthogonal to the plane of incidence and parallel to the plane of the surface, and the p-component is in the plane of incidence. An image of this reflection geometry is illustrated in Figure 2.7.

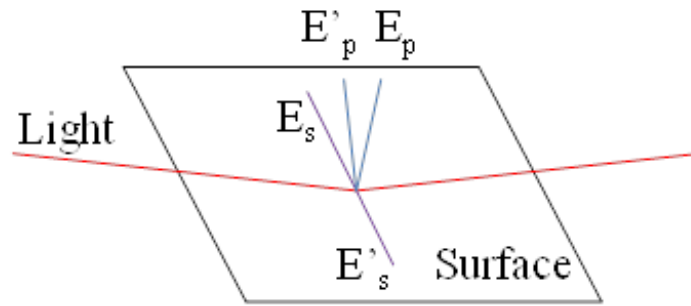


Figure 2.7 A drawing of the reflection geometry of the electric field components of infrared light. E and E' represent the incident and reflected electric fields, respectively, and s and p represent the s and p components of the electric field.

The electric field at the surface is defined as:⁹⁵

$$E = E^i[\sin\theta + r\sin(\theta + \delta)] \quad (2)$$

where θ is the phase angle, r is the reflection coefficient, i indicates incident, and δ is the phase of the reflected wave. The first term of the equation represents the amplitude of the incident electric field, and the second term of the equation represents the amplitude of the reflected electric field.⁹⁵ In the above image, it can be seen that for all angles of

incidence, the field of the s–component remains parallel to the surface, which results in an r value of ~ 1 for all angles of incidence. Also at all incidence angles, the δ value remains close to 180° .⁹⁵ As seen in the equation above, this leads to destructive interference of the reflected wave, therefore, illustrating that the s–component does not interact with the adsorbate.

The p–component has radiation that is parallel and normal to the surface. The parallel and perpendicular electric fields of the p–component are:⁹⁵

$$E_p^{\parallel} = E_p^i \cos\phi [\sin\phi - r_p \sin(\theta + \delta_p)] \quad (3)$$

$$E_p^{\perp} = E_p^i \sin\phi [\sin\theta + r_p \sin(\theta + \delta_p)] \quad (4)$$

where ϕ is the grazing incidence angle. The parallel components will yield a relatively small electric field since these components are opposite in direction to the surface normal. As seen in equation (3), due to the $\cos\phi$ term, the parallel components will be the greatest at small angles. The perpendicular or normal components will constructively interfere as seen in equation (4). Due to the $\sin\phi$ term, the parallel components will decrease and the perpendicular components will increase as the grazing incidence angle increases. Hence, only the perpendicular component of the p–component contributes to the surface electric field.

The intensity of a RAIRS signal is described by the expression:⁹⁵

$$\text{Intensity} = \Delta R = \left(\frac{E_p^{\perp}}{E_p^i} \right)^2 \sec\phi \quad (5)$$

where $\left(\frac{E_p^\perp}{E_p^\parallel}\right)$ is the amplitude of the electric field. This equation shows that only the perpendicular component of the p polarized light influences the RAIRS signal and that the larger the grazing incidence angle, ϕ , the greater the produced signal. In addition, experiments have shown that RAIRS is more efficient at shorter wavelengths (e.g., 2100 cm^{-1}) versus longer wavelengths (e.g., 500 cm^{-1}) and that ΔR has the greatest value when the sample is highly reflective.⁹⁵ Another way to interpret the surface selection rule for RAIRS experiments is by using image dipole theory. A picture representing the general principle of image dipole theory is shown in Figure 2.8.

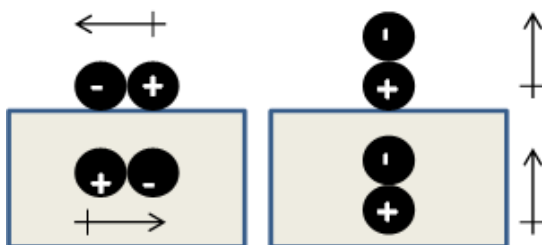


Figure 2.8 A schematic of the dipole moments of the vibrational modes of a molecule and the image dipole. (Left) represents parallel dipole moments and (right) represents perpendicular dipole moments.

When a dipole moment of vibration interacts with a conductive surface, electrons in the near-surface region of the solid rearrange themselves so that they are directed towards the positive end of the dipole moment. The region that was previously occupied by the redirected electrons is now positively charged (i.e., a “hole”), creating a so-called image dipole. When the dipole of the molecular vibration is perpendicular to the plane of the surface, the image dipole vectors will also point perpendicular to the surface. By vector addition, this will give an enhanced signal for this type of vibrational motion. In

contrast, if the dipole moment of the molecular vibration is parallel to the plane of the surface, the image dipole vector will be equal in magnitude and opposite in direction. Thus, the vectors will cancel and no infrared signal will be detected in this case. This phenomenon explains why the net dipole moment increases when the dipole moment and the image dipole are perpendicular to the plane of the surface, and why the net dipole moment is zero when the dipole moment and image dipole are parallel to the plane of the surface.

2.3.2 Vibrational Frequencies and Line Shapes

It is useful to include a brief discussion on the shift in frequency that is seen in almost all the RAIRS data presented in this thesis. The change in the frequency as the dosage increases is attributed to dipole coupling, chemical shifts and/or hydrogen bonding.^{96,97,98} The phenomenon of dipole coupling occurs when oscillators are close to each other (e.g., on a surface). The dipoles become coupled and an in-phase mode (with a frequency of $\omega_0 + \Delta\omega$) and an out-of-phase mode (with a frequency of $\omega_0 - \Delta\omega$) are produced.⁹⁶ Since only the in-phase mode is dipole active, this provides an explanation for why the peaks tend to blueshift. Chemical shifts, which are a result of the change in the electronic environment at the interface, occur in conjunction with dipole coupling and are likely influencing the shift in frequency observed in the results presented here.

A variety of line shapes are also illustrated in the RAIRS data. Therefore, a discussion based on the work by Hoffmann⁹⁹ on the theory of RAIRS line profiles will be mentioned. Homogeneous and inhomogeneous line broadening are typically observed in experimental data. Homogeneous line broadening arises when the vibration at the interface is dampened by the coupling of phonons to vibrational modes and/or

electron–hole pair creation. In electron–hole pair creation, electron–hole pairs get excited and subsequently relax, which is suggested to cause lifetime broadening. Inhomogeneous broadening provides more information on the adsorption site and intermolecular interactions and is sensitive to low coverage versus high coverage behavior. RAIRS data of low coverage experiments are dependent on the surface mobility (which is dependent on temperature) and repulsive/attractive intermolecular forces. A display of common line profiles appearing at low coverage is shown in Figure 35 of Hoffmann reference.⁹⁹ High coverage behavior is mainly governed by intermolecular repulsion, and the magnitude of intermolecular repulsion is dependent on low and high surface diffusion barriers.

2.4 Carbon Monoxide Adsorption Technique

Carbon monoxide (CO) has its Highest Occupied Molecular Orbital (HOMO) as the 5σ bonding orbital, and the orbital has its largest lobe on the backside of the carbon atom, making CO bond to a metal in an upright position. In the upright position, the principle axis of the molecule is perpendicular to the plane of the surface, with the C atom attached to the surface and the O atom extended in the vacuum. This 5σ orbital has electrons that are able to be donated in a sigma fashion to an orbital in the metal atom. The Lowest Unoccupied Molecular Orbital (LUMO) in CO is the $2\pi^*$ antibonding orbital, and the orbital has lobes on carbon and oxygen. If the metal has electrons in a d-orbital of appropriate symmetry to overlap with the antibonding orbital of CO (i.e., $d\pi$ orbitals), then the metal is able to donate electrons back to CO, in a so-called pi backbond.

The effect of CO being a strong sigma donator and a strong pi acceptor is synergistic. The more electron density CO donates to the metal, the more electron rich the

metal becomes, and the more electron density the metal is able to donate back to CO. This effect causes the metal–carbon bond to strengthen and the carbon–oxygen bond to weaken. The weakening of the CO bond means it is lower in energy, which causes a red–shift in the CO stretching frequency. Hence, the CO frequency can provide identification of the probed metal species.¹⁰⁰

The sensitivity of the CO vibrational frequency makes it a popular probe molecule in surface analysis.⁹⁴ The CO stretching frequency is dependent on a number of factors, including the nature of the metal, the adsorption geometry of CO and the CO coverage.^{94,100,101}

2.5 Temperature Programmed Desorption

Temperature programmed desorption (TPD) is a technique useful in determining the energy of desorption, the Arrhenius pre–exponential factor (A) and the desorption order.^{55,56,93} Additionally, TPD aids in identification of the desorbed products and helps in the interpretation of RAIRS data. Hence, qualitative and quantitative information can be extracted from TPD data.

The desorption order can be obtained by using the Polanyi–Wigner formula:⁹³

$$r_{des} = \frac{-d\theta}{dt} = v_n \theta^n \exp\left(\frac{-E_{des}}{RT}\right) \quad (6)$$

where r_{des} is the desorption rate, θ is the concentration of adsorbate molecules on the surface, v_n is the desorption pre–exponential factor, n is the desorption order, E_{des} is the desorption energy, R is the gas constant, T is the temperature of the substrate and t is

time. In a temperature programmed desorption experiment, the temperature is raised linearly as a function of time from an initial temperature:¹⁰²

$$T = T_0 + \beta t \text{ and } dT = \beta dt \quad (7)$$

where T is the temperature of the substrate, T_0 is the temperature at $t = 0$ and β is the heating rate. The Polanyi–Wigner formula can then be written as a function of the heating rate by substituting $\frac{dT}{\beta}$ for dt in (6):⁹³

$$\frac{-d\theta}{dT} = \frac{v_n \theta^n \exp\left(\frac{-E_{des}}{RT}\right)}{\beta} \quad (8)$$

To study the relationship between temperature and the other variables, it is useful to remember that the maximum value for r_{des} is found when the gradient of the TPD curve is equal to zero. In that regard, the derivative of Equation (8) with respect to temperature can be set to zero. After rearrangement of the variables, a new equation is derived:

$$\frac{E_{des}}{RT^2} = \frac{v_n}{\beta} \exp\left(\frac{-E_{des}}{RT}\right) \quad (9)$$

Equation (9) shows that the temperature corresponding to the maximum value of the TPD curve is proportional to E_{des} and β , and inversely proportional to v_n . In other words, when E_{des} is shifted to a higher energy, the TPD peak will be shifted to a higher temperature.

To determine E_{des} , incorporation of the natural log into Equation (6) will result in Equation (10):

$$\ln(r_{des}) = n \ln(v_n \theta^n) - \frac{E_{des}}{R} \frac{1}{T} \quad (10)$$

An Arrhenius plot can be made to determine the activation energy, where the x-axis is $\frac{1}{T}$, the y-axis is $\ln(r_{des})$, the y-intercept (b) is $n \ln(v_n \theta^n)$ and the slope (m) is $-\frac{E_{des}}{R}$.

When performing a TPD experiment, it is important to know that the desorption temperature can provide information about the adsorbate–surface interaction. Adsorbates can chemisorb (bind through a covalent interaction), physisorb (bind through intermolecular forces such as a van der Waals interaction), desorb, readsorb, decompose before desorption, desorb from various binding sites and/or be formed by recombination.⁵⁶ For example, low temperature desorption usually indicates physisorption. Desorption at higher temperatures typically suggests that the desorbing species results from a reaction (e.g., recombinative desorption) on the surface.

2.6 Scanning Electron Microscopy and Energy Dispersive X-ray Spectroscopy

A scanning electron microscope (SEM) coupled with an energy–dispersive X–ray spectrometer (EDS) can provide information on the geometric structure of the surface as well as the elemental composition. Depending on the type of electron gun used, relatively large defect sites to individual surface atoms can be observed,¹⁰³ which makes SEM/EDS ideal to observe the complex structure of mineral surfaces. The instrument used to measure the spectra reported in this thesis has a resolution of approximately 1 nm at 1.0 kV.

The scanning electron microscope can detect secondary electrons, and that detection provides information on the morphology of the surface.¹⁰⁴ Secondary electrons are low-energy electrons that are a few nanometers away from the surface, therefore, detection of secondary electrons results in an image of the surface of the sample. The process of yielding secondary electrons begins with using an electron gun, which irradiates the sample via electrons at a chosen accelerating voltage. This causes valence electrons from the sample to be emitted into vacuum and eventually guided to an Everhart-Thornley detector (*n.b.*, that only valence electrons near the surface can be emitted due to the low energy of secondary electrons). A bright spot in the image indicates that relatively more secondary electrons have escaped from that region, and a dark spot in the image indicates that relatively fewer secondary electrons have escaped from that region. Not only does this phenomenon result in a perceptibly defined geometric structure of the surface, but it also illustrates which regions are flat versus composed of edges, since edges tend to emit more electrons and appear brighter.

Energy-dispersive X-ray spectroscopy (EDS) allows identification of chemical species, at the surface and below, to around 1 micrometer. Unlike secondary electron imaging, the EDS technique utilizes high-energy electrons to eject an electron from an inner shell of each atom. After this occurs, an outer shell electron fills the vacancy, which causes the release of an X-ray with energy that is unique to the atomic structure of the targeted atom. Due to matrix effects, the values of the atomic percentages must be examined closely. The intensity ratio for each characteristic energy is influenced by factors such as X-ray absorption, X-ray fluorescence and electron backscattering. In

addition, EDS is not sensitive enough to probe trace elements or light elements (typically elements lighter than sodium), making EDS a semi-quantitative technique.¹⁰⁴

An advantage of EDS is that it can map the distribution of elements on a sample, also known as elemental mapping. In elemental mapping, a selected region is raster scanned by a high-energy beam to identify the elements in that region. Since X-ray counts are measured per image pixel,¹⁰⁵ the map is essentially a pixelated image with colors that correspond to each X-ray line. Since each X-ray line corresponds to a unique atomic structure, the map subsequently illustrates the spatial distribution of elements across a region. This technique allows the user to identify the location of the binding sites relative to the geometric structure of the sample, as well as identify diffusion of the elements.

2.7 X-ray Photoelectron Spectroscopy

X-ray photoelectron spectroscopy (XPS) can identify oxidation states and quantitate the composition of the sample with a sampling depth of approximately 10 nm.^{106,107} These traits illustrate that XPS provides direct information on the identification and quantification on the composition of the surface.

When an incoming photon is absorbed by a surface atom, a photoelectron is emitted if the incoming photon has an energy greater than the binding energy of the emitted electron (i.e., photoelectron). This can be described mathematically:

$$E_B = h\nu - E_k \quad (11)$$

where E_B is the electron binding energy (also referred to as the work function and

designated by the symbol Φ), $h\nu$ is the energy of the incoming photon and E_k is the electron kinetic energy. Deep-core electrons need X-ray energies in order to be emitted from the solid and into vacuum due to their relatively high binding energies.

Depending on the oxidation state of the atom and the substituents bound to the atom, E_B will shift. This shift is called a chemical shift and is symbolized as ΔE_B . If the oxidation state increases, the binding energy will increase. If there are electron withdrawing substituents, the binding energy will increase as well. Essentially, the more electronegative the atom is, the greater the increase in the chemical shift.

The width of XPS peaks is governed primarily by lifetime broadening, which produces a Lorentzian profile. According to the Heisenberg uncertainty relation:

$$\Gamma = \frac{h}{\tau} \quad (12)$$

where h is Planck's constant, τ is the lifetime of the core hole and Γ is the peak width. The lifetime of the core hole decreases as the core hole gets deeper (i.e., as the core hole gets closer to the nucleus) since there are more electrons available to fill the hole. Therefore, at a given shell energy level, the greater the atomic number, the more electrons there are available to fill the hole, which consequently decreases the lifetime and increases the linewidth. Because deep-core electrons do not participate in bonding and have energies that are intrinsic to the atom, the peak area is proportional to the number of atoms.

2.8 Development of a Synthetic Schreibersite Sample and Iron–Nickel Control for Surface Science Analysis

To our knowledge, this is the first RAIRS study of a metal phosphide. Because RAIRS requires a surface that is both reflective in the infrared region and also has sufficient conductivity to allow an image dipole to be created, it has typically been performed on single-crystal metal surfaces or thin metal-oxide films grown on metals. Although they are not metals, iron and nickel phosphides have been characterized as very low band gap materials (i.e., 0.50 eV or less)^{108,109,110} and they have a metallic luster when polished. Unfortunately, iron–nickel phosphides are not available commercially and there is currently no procedure for growing single crystals. The procedure for creating the smooth solid samples necessary for a RAIRS measurement is outlined below.

The synthetic schreibersite sample had a composition of $(\text{Fe,Ni})_3\text{P}$. Powders of iron, nickel and red phosphorous (2:1:1) were heated under an argon atmosphere at 820°C for 235 hours by N. La Cruz.¹¹¹ The sample was then pulverized, sieved and pressed into an iron plate with a hydraulic press capable of applying 20 tons of pressure. To form a robust solid sample, the sample was sintered under an argon atmosphere at 950°C for one hour. Pressing under high pressure and sintering was necessary because iron–nickel phosphides are both very hard and very brittle. The history of the sample is shown in Figure 2.9.

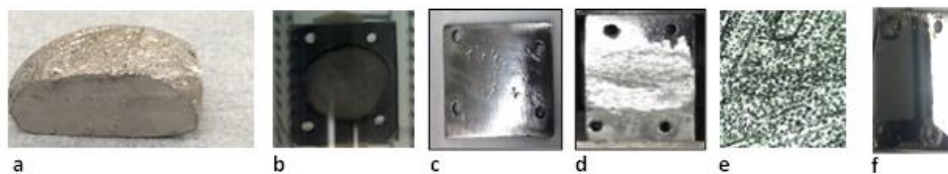


Figure 2.9 (Left to right) Schreibersite samples after (a) heating Ni, Fe and P powders under Ar in a tube furnace at 820°C for 235 hours, (b) pressing pulverized and sieved FeNi₂P into an iron plate, (c) polishing with a wire-brush attachment on a Dremel and using Pikal powder, (d) milling the surface, (e) same as (d) but under 100x magnification, and (f) polishing with a roll grinder and grinder-polisher.

Characterization of the sample throughout the development procedure was conducted by XPS and SEM coupled with EDS in order to identify elements near the surface and observe the geometric arrangement of the surface. As seen in Figure 2.10, phosphorus was segregated across the sampling region. X-ray diffraction data indicates that the phosphorus depleted areas were iron-nickel alloys.¹¹¹ This segregation was most likely caused by heating the sample to 950°C during sintering.

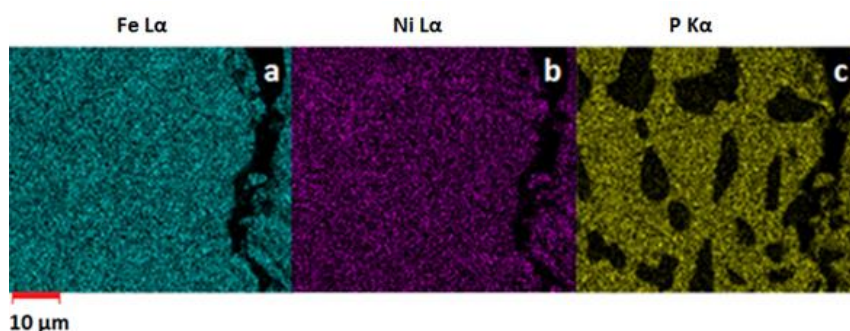


Figure 2.10 Elemental maps of the L α lines of (a) iron, (b) nickel and (c) phosphorus superimposed on a secondary electron image of a region of the sample. Images were taken with the Hitachi SU8230 Cold Field Emission SEM/EDS system. An accelerating voltage of 10 kV was used.

To flatten and polish the sample, the sample was first smoothed with 60-grit sandpaper and then with 120-grit sandpaper on a roll grinder (Buehler HandiMet 2). The sample was further flattened with 180-grit sandpaper using a grinder-polisher (Buehler EcoMet 300). The grinder-polisher was set at 250 rpm and the sample was pressed against the sand paper with a pressure of 5 psi for 2 minutes. This step was repeated using 320-grit sandpaper. To polish the sample to a mirror-finish, 9 μm diamond suspension was sprayed onto an ultrapad cloth and the sample was pressed against the cloth for 5 minutes at 5 psi with the grinder-polisher set at 150 rpm. This step was repeated with 3 μm and 1 μm diamond suspension sprayed on trident cloth, followed by a 0.05 μm alumina suspension sprayed on microcloth. Images of the sample before and after flattening and polishing are shown in Figure 2.11.

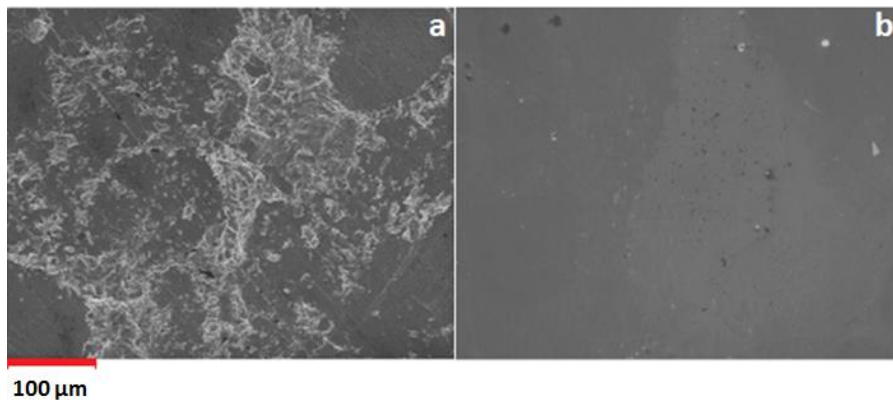


Figure 2.11 (a) Secondary electron images of the surface before flattening and polishing the schreibersite surface and (b) after flattening and polishing the surface with Buehler products.

The lack of bright features in (b) is an indicator of the reduction of edges within the probed area because the probability that an electron will escape from an edge is higher than the probability that an electron will escape from a flat terrace. Yet, the

surface has numerous defect sites and, therefore, is similar to the mineral's naturally rough topography.

The alumina suspension left cloudy-colored contamination on the sample that was visible to the naked eye, as seen in Figure 2.12. In an effort to remove the contamination, the sample was polished again using the same procedure without the alumina suspension. The sample was then imaged by a scanning electron microscope (SEM) and the composition of the sample at a depth of 1 μ m below the surface was analyzed by an energy dispersive spectrometer (EDS) in order to verify whether the contaminant was present or no longer present. Table 2.1 lists the atomic percentages obtained by EDS. According to the SEM/EDS data, there were trace amounts of contamination.

An iron–nickel sample was created as a control by T. Beckman. Beckman pressed FeNi powder in a brass bushing with steel anvils at 20 tons, sintered the pressed powder in a tube furnace that was initially under vacuum and then further purged with argon, and finally set the disk within a steel plate and polished the disk and plate with a rotary grinder until a mirror finish was achieved.

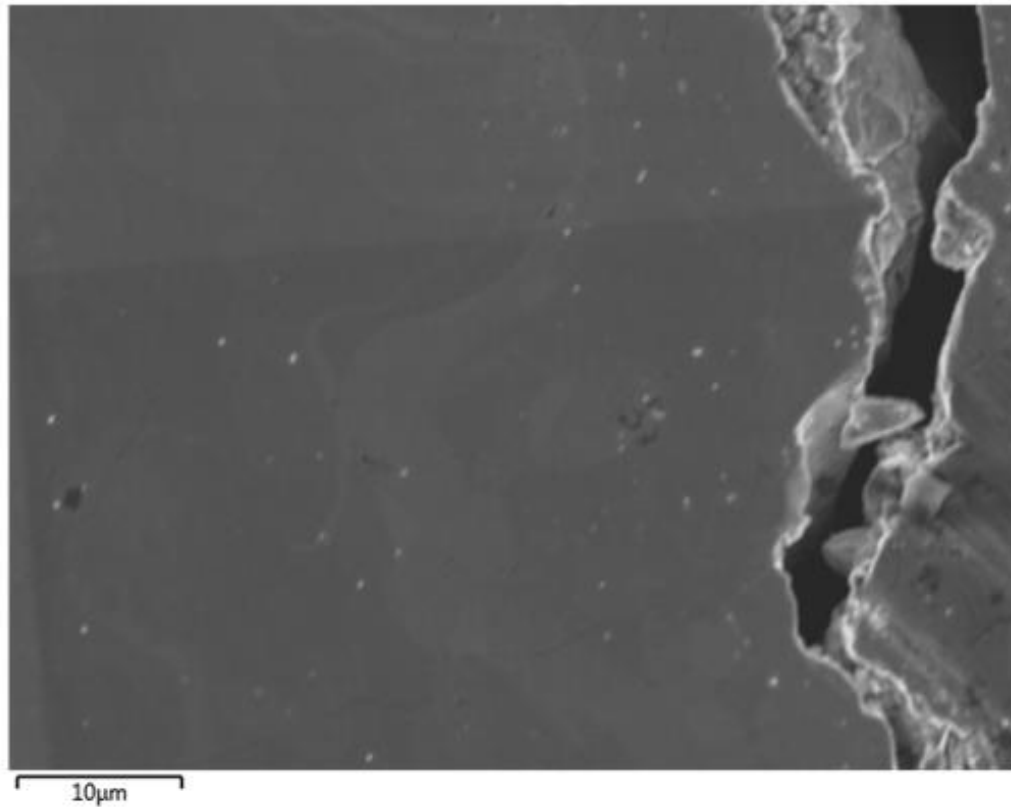


Figure 2.12 Representative Scanning Electron Microscope (SEM) image of the surface of the schreibersite sample after polishing with alumina suspension. Cloudy-colored swirls can be seen on the surface at 21000x magnification.

Table 2.1 Atomic percent of elements within the sample (+/- 0.5% uncertainty) obtained by EDS.

element	atomic %
Fe	53.4
Ni	15.8
P	18.1
C	9.7
O	2.6
Al	0.2
Si	0.2

After SEM/EDS analysis, XPS was performed to complement the EDS data as well as reveal the composition of the sample to a depth of 10 nm below the surface. Figure 2.13 shows an XPS spectrum of the Fe₂NiP sample, and Table 2.2 lists the normalized atomic percentages representing that sampling region.

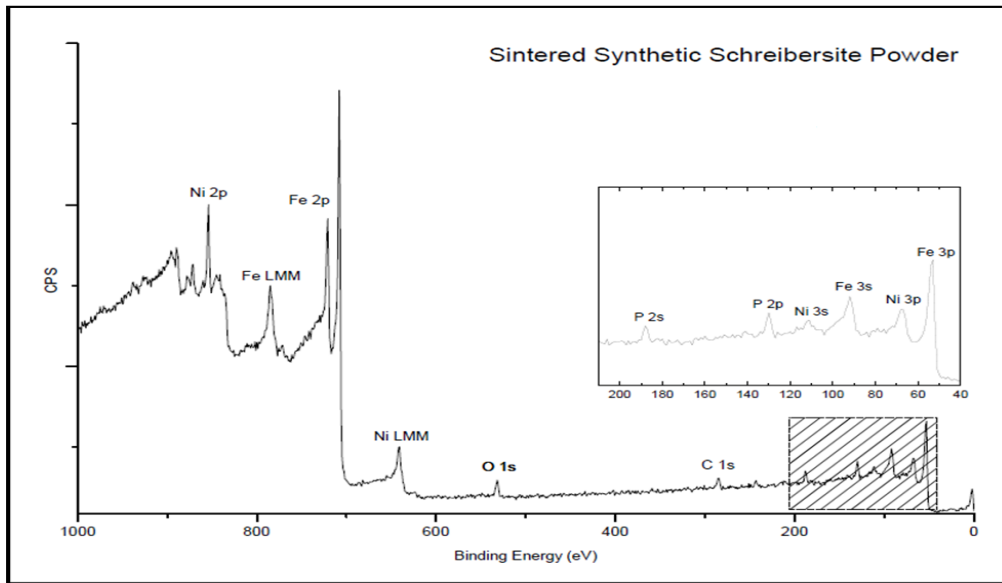


Figure 2.13 XPS of the unpolished Fe₂NiP sample. *Image Credit: A. McKee, T. Orlando Group, Georgia Institute of Technology.*

Table 2.2 Normalized data of the atomic percent of elements within the sample (+/- 0.5% uncertainty) obtained by XPS.

element	atomic %
Fe 3p	55.8
Ni 3p	22.2
P 2p	12.6
O 1s	9.4

Because the data in Table 2.1 is unnormalized and the data in Table 2.2 is normalized, it is difficult to compare the two. However, it is evident that more phosphorus was detected by the EDS than the XPS, suggesting that there is a higher abundance of phosphorus further below the surface. It is possible that the depletion of surficial phosphorus was caused by oxidation via exposure of the sample to air, which would, if true, demonstrate the reactive nature of phosphorus in schreibersite.

CHAPTER 3: WATER AND HYDROGEN PEROXIDE ON SCHREIBERSITE

3.1 RAIRS Data and Analysis of Water on Fe₂NiP and FeNi at Low Surface Temperatures (H₂O, H₂¹⁸O and D₂O)

Low temperature (Temperature (T) = 125 K) and high temperature (T = 295 K) studies of water (H₂O) adsorbed to Fe₂NiP were performed to observe the influence of the mineral surface temperature on the chemistry at the interface. To aid with peak assignment, several control experiments were conducted. For the low temperature experiments, these controls include D₂O adsorbed to Fe₂NiP, H₂¹⁸O adsorbed to Fe₂NiP and H₂O adsorbed to FeNi.

The proposed adsorption geometry of H₂O on the schreibersite surface is shown in Figure 3.1 and is supported by the following discussion. Figure 3.2 shows the growth of vibrational bands as the exposure of H₂O on a synthetic Fe₂NiP surface is increased. The frequencies observed in Figure 3.2 were assigned by comparison to RAIRS data of other model systems that are relevant to our experiments, e.g., ices on nickel, iron, nickel oxide and iron oxide surfaces. This comparison is outlined in Table 3.1. Experimentally observed RAIRS frequencies and their relative intensities are: 3445–3425 cm⁻¹ (strong), 892–812 cm⁻¹ (medium) and 1226 cm⁻¹, 1710–1548 cm⁻¹, 2257–2170 cm⁻¹ (weak). The peak at ~3400 cm⁻¹ is assigned to the hydrogen–bonded O–H stretch of H₂O since the free (non hydrogen–bonded) O–H stretch has a stretching frequency of ~3580 cm⁻¹ for H₂O adsorbed on oxidized iron surfaces.⁶⁹ Since hydrogen bonding lowers the potential energy of the OH potential well,¹¹² the hydrogen–bonded O–H stretch has a lower

frequency than the free O–H stretch. By comparison of the frequencies to the reference values listed in Table 3.1, the H₂O is most likely bound to an iron site versus a nickel site.

Since the interaction of H₂O with phosphorus is a main interest in this study, an iron–nickel control sample was created. It is assumed that a distinction in the RAIRS frequencies and line profiles between the Fe₂NiP experiments and the FeNi experiments is due to differences resulting from the incorporation of phosphorus. These differences could be the result of the adsorbate molecules interacting with P atoms in the surface or they could be the result of changes in the electronic structure of the solid as a result of P incorporation (i.e., synergistic effects). Figure 3.3 illustrates RAIRS data of H₂O at various exposures on an FeNi sample. The shift of the O–H stretching frequency to ~3390 cm⁻¹ in Figure 3.3 from ~3450 cm⁻¹ in Figure 3.2 suggests that H₂O is interacting with phosphorus at the interface. To determine if oxidation or reduction occurs at the Fe₂NiP surface, H₂¹⁸O and D₂O control experiments were conducted. Figure 3.4 shows the adsorption of H₂¹⁸O on Fe₂NiP and Figure 3.5 shows the adsorption of D₂O as probed by RAIRS. The isotopic shift of the O–H stretching frequency can be seen by comparing the peak at ~3400 cm⁻¹ in Figure 3.4 to the peak at ~3450 cm⁻¹ in Figure 3.2.

Unfortunately, this isotopic shift does not provide insight as to whether the oxygen atom or the hydrogen atoms interact with the surface. However, it is likely that the oxygen atom is bound to the surface and the hydrogens are extended into the vacuum due to the lone pair on the oxygen. The shoulders along the OH peak in Figures 3.2, 3.3 and 3.4 indicate small island formation of amorphous H₂O ice on the surface in all cases.^{99,113}

The libration mode for H₂O observed at 892 – 812 cm⁻¹ also suggests that H₂O ice is on the surface. Since the libration mode is a result of the molecule undergoing a “frustrated

rotation” due to being trapped in the ice, the mode is not highly sensitive to the interaction between the adsorbate and the mineral surface. Thus, the frequency shift of the libration mode when H₂O is adsorbed on FeNi versus Fe₂NiP is relatively low compared to the frequency shift observed for the O–H stretching mode.

The H₂O bend at ~1700–1500 cm⁻¹ and the peak at ~2200–2100 cm⁻¹ are weak transitions and, therefore, the isotopic and chemical shifts are difficult to distinguish. At 0.6 L, two peaks for the H₂O bend arise, and this phenomenon is suggested to be a result of inhomogeneous broadening caused by surface domains of different order.⁹⁹ To our knowledge, there are no references for H₂O adsorption on iron, iron oxides, nickel and nickel oxides that contain transitions at ~2200–2100 cm⁻¹. It is hypothesized that this peak is a combination band and/or overtone that is related to the interaction with iron and/or nickel since the peak appears in the FeNi control experiment. It is also possible that this feature is related to CO₂, since the C–O stretch for an unpurged system would be in this area. Because the intensity of the infrared beam was no less than the intensity of the infrared beam in the H₂O experiments, this issue is not a function of the amount of light detected by the detector.

The transition at ~1220 cm⁻¹ in all the Fe₂NiP experiments is not native to the infrared features of H₂O adsorption on iron, iron oxides, nickel or nickel oxides and is commonly assigned to the P=O stretch.^{114,115,116,117,118} However, it could also represent the C–O stretch or the O–C–O bend if organic contamination is present.^{83,119} A number of control experiments were performed to elucidate the nature of the band. As mentioned previously, the weak ~1220 cm⁻¹ feature in the H₂¹⁸O data made it difficult to observe the

isotopic shift and, therefore, was not helpful in understanding the origin of that peak in the H₂O data. Unfortunately the D–O–D bend is at 1200 cm⁻¹,¹²⁰ which also made the D₂O experiment not useful for this situation. Future experiments using HDO could help with this assignment. The mystery peak did not show up in the H₂O adsorption on FeNi data, but it did show up in the CH₃OH adsorption on FeNi experiment discussed in Chapter 4.

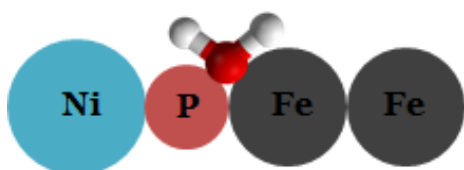


Figure 3.1 Proposed adsorption geometry of H₂O on Fe₂NiP at a surface temperature of about 130 K.

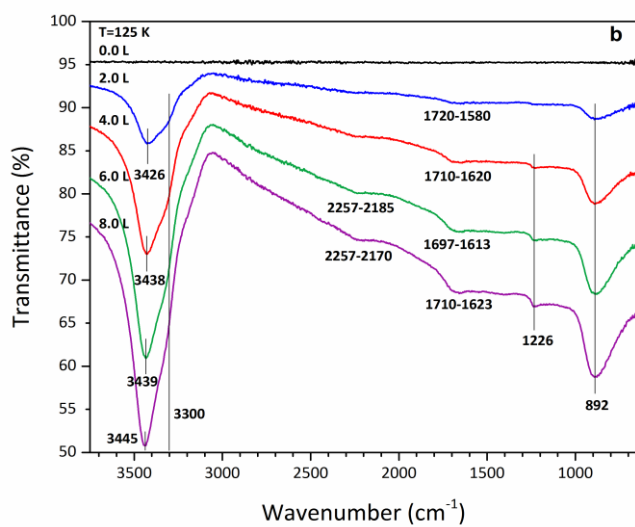
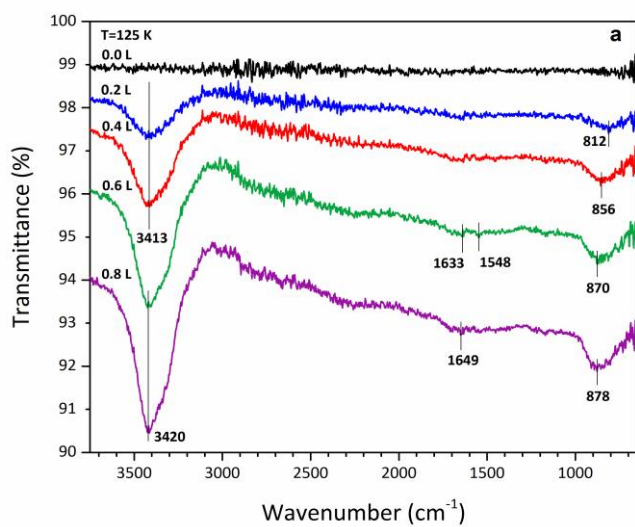


Figure 3.2 (a) A RARS spectra of H₂O adsorbed to Fe₂NiP with a H₂O dosage of 0.2 L – 0.8 L and (b) 2.0 L – 8.0 L. Experiments were run with a sample temperature of 125 K.

Table 3.1
 Vibrational frequencies (cm^{-1}) of H_2O adsorbed to Fe_2NiP at a H_2O dosage of 0.2 L – 8.0 L and a sample temperature of 125 K. Frequencies from other experiments are also shown.

dosage (L)	band assignment	this exp	other exp (iron/iron oxide substrate)	other exp (nickel/nickel oxide substrate)
0.2–8.0	H_2O libration	892–812	820–800, ^a 930, ^b 690 ^c	760–530 ^d
0.2–8.0	Unknown	1226		
0.2–8.0	H–O–H scissors	1710–1548	1630–1620, ^a 1600, ^{a,b} 1630 ^c	1610–1570 ^d
0.2–8.0	Unknown	2257–2170		
0.2–8.0	OH stretch	3445–3425	3420 ^d	3300 ^e

^aReference 69. ^bReference 70. ^cReference 72. ^dReference 71. ^eReference 68.

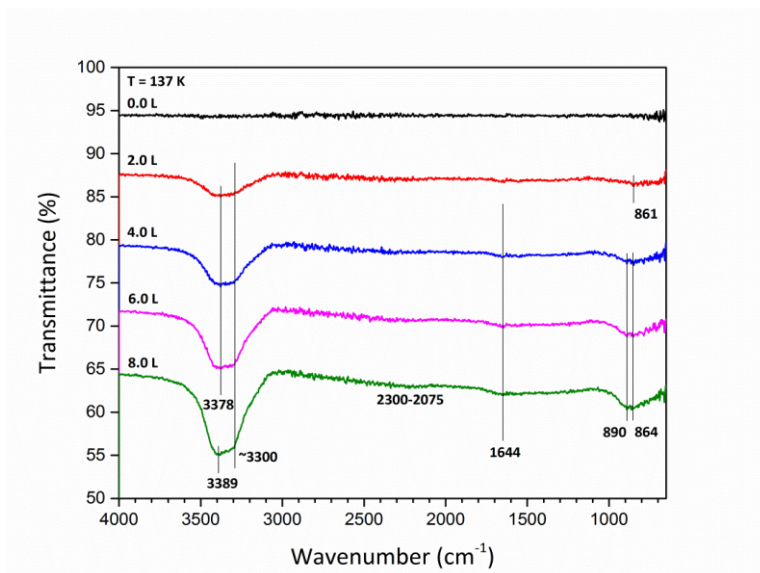


Figure 3.3 A RAIRS spectra of H₂O adsorbed to FeNi control sample with a H₂O dosage of 2.0 L – 8.0 L. Experiments were run with a sample temperature of 137 K.

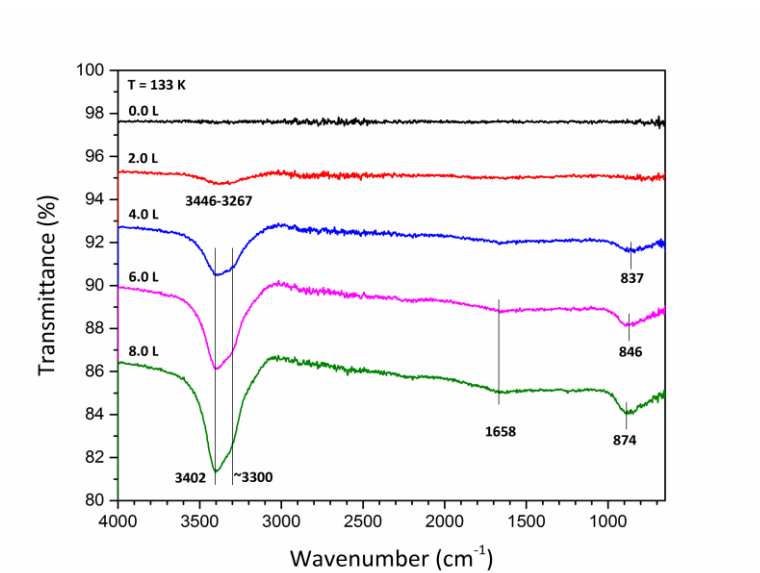


Figure 3.4 A RAIRS spectra of H₂¹⁸O control molecule adsorbed to Fe₂NiP with a H₂¹⁸O dosage of 2.0 L – 8.0 L. Experiments were run with a sample temperature of 133 K.

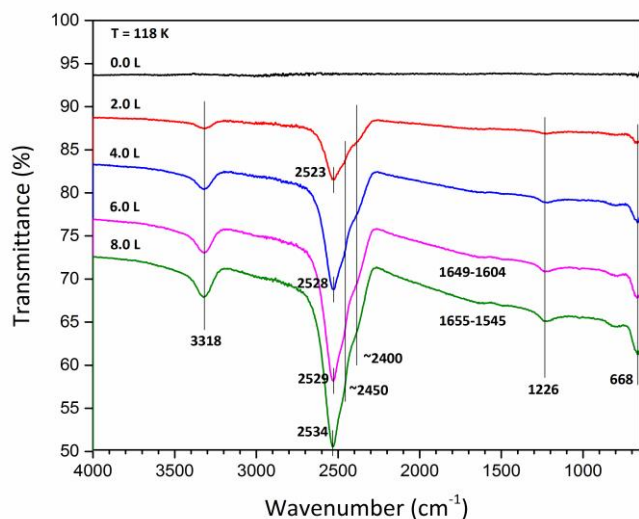
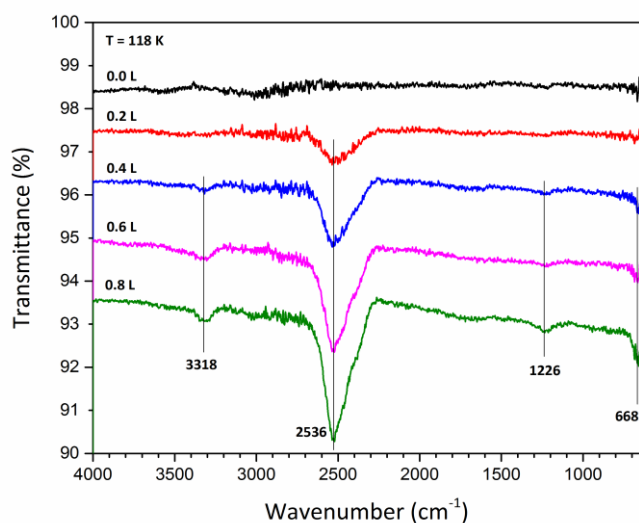


Figure 3.5 (a) A RAIRS spectra of D₂O control molecule adsorbed to Fe₂NiP with a D₂O dosage of 0.2 L – 0.8 L and (b) 2.0 L – 8.0 L. Experiments were run with a sample temperature of 118 K.

To eliminate the possibility that the peak is representative of organic contamination, a significant effort was made to clean the surface within the UHV chamber. Figure 3.6 shows RAIRS data of H₂O on Fe₂NiP after 3 cycles of argon ion bombardment (30 minutes at 5.0×10^{-5} torr) and flashing cycles (550 K set-point

temperature), which resulted in the disappearance of the $\sim 1220\text{ cm}^{-1}$ band. This supports a conclusion that the H_2O source itself does not contain organic contamination.

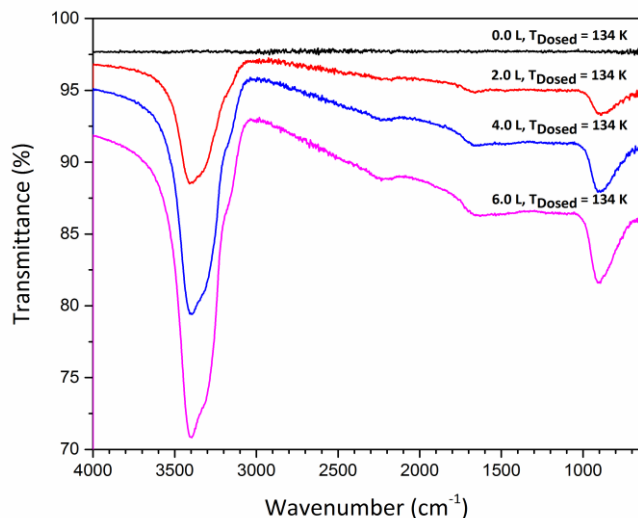


Figure 3.6 A RAIRS spectra of H_2O adsorbed to Fe_2NiP with a H_2O dosage of 2.0 L – 6.0 L. The experiment was performed one day after argon ion bombardment and flashing cycles.

The next day, one argon ion bombardment experiment was performed without flashing before H_2O was dosed onto the surface, and that experiment is exhibited in Figure 3.7. The $\sim 1220\text{ cm}^{-1}$ band appeared, which suggests that the peak could be a result of corrosion by H_2O or an increase in the energy of the surface atoms due to argon ion bombardment alone (*n.b.*, no heat addition or flashing was performed for the data shown in Fig. 3.7), which would have promoted surface relaxation to a thermodynamically more stable structure.

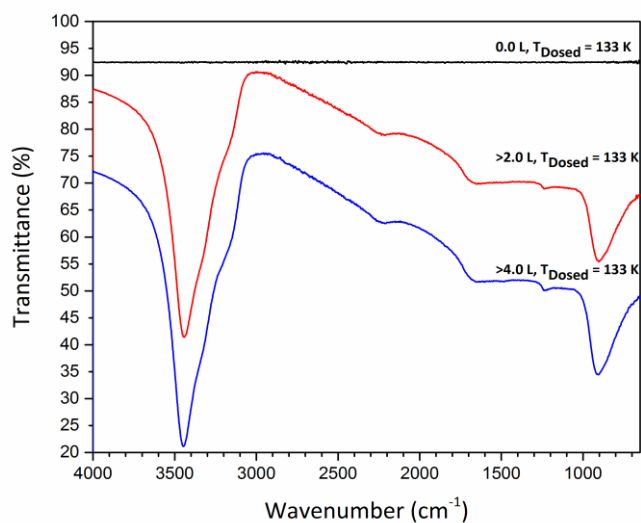


Figure 3.7 A RAIRS spectra of H₂O adsorbed to Fe₂NiP with a H₂O dosage of ~2.0 L – 4.0 L. An estimate on the dosage is due to the malfunction of the leak valve during the experiment. The experiment was performed two days after argon ion bombardment and flashing cycles and one day after a H₂O experiment.

Figure 3.8 shows a H₂O experiment conducted two days after argon ion bombardment and flashing cycles without performance of experiments in between to determine if the peak is due to a corrosion process. The disappearance of the ~1220 cm⁻¹ peak suggests that the peak does not represent a product of corrosion.

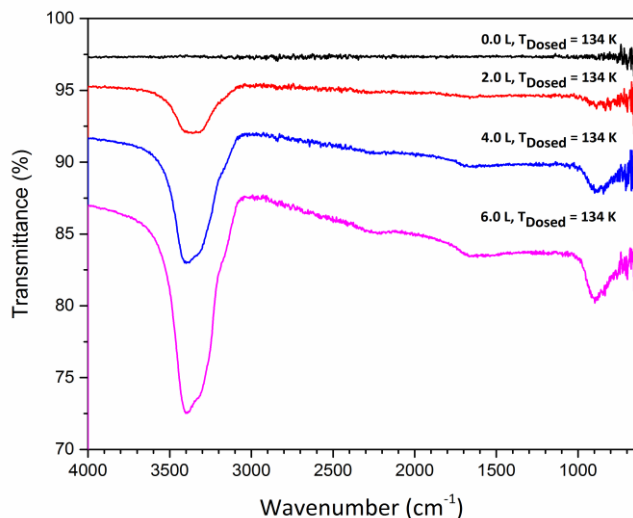


Figure 3.8 A RARS spectra of H₂O adsorbed to Fe₂NiP with a H₂O dosage of 2.0 L – 6.0 L. The experiment was performed two days after argon ion bombardment and flashing cycles with no experiments performed in between the two days.

To investigate if argon ion bombardment has a role in the production of the puzzling $\sim 1220\text{ cm}^{-1}$ species, a H₂O experiment was done the next day after one argon ion bombardment experiment without flashing, and that experiment is represented in Figure 3.9. As seen in the figure, the transition did not appear. Future work on clarifying the nature of this peak includes reducing the chamber pressure to eliminate the possibility of contamination within the chamber (e.g., from pump oil or other carbon deposits building up on the surface over time).

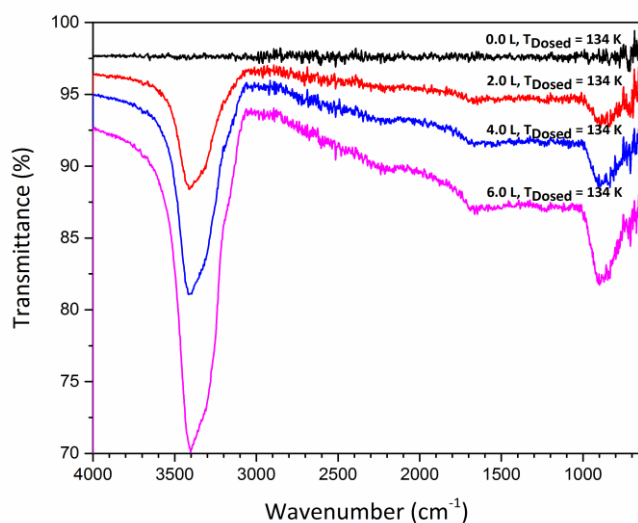


Figure 3.9 A RAIRS spectra of H₂O adsorbed to Fe₂NiP with a H₂O dosage of 2.0 L – 6.0 L. The experiment was performed two days after argon ion bombardment and flashing cycles with no experiments performed in between the two days, and one day after H₂O was dosed on the surface.

3.2 RAIRS Data and Analysis of Water on Fe₂NiP and FeNi at High Surface Temperatures (H₂O)

RAIRS spectra of the synthetic schreibersite surface before (black spectrum) and after (blue and red spectra) exposure to H₂O are shown in Figure 3.10. H₂O was dosed while the surface temperature (T_{Dosed}) was held at 130 K (blue spectrum) and 295 K (red spectrum). All RAIRS spectra were collected at a surface temperature of 130 K or lower to produce a steady baseline. The experiment with $T_{\text{Dosed}} = 295$ K (red spectrum) required a higher dosage than the experiment with $T_{\text{Dosed}} = 130$ K (blue spectrum) because the molecular sticking coefficient of H₂O in vacuum is lower at the higher surface temperature. For $T_{\text{Dosed}} = 295$ K (red spectrum), the peak at 3187 cm⁻¹ indicates dissociative chemisorption of H₂O as hydroxyl (OH⁻).¹²¹ The peak at 2423 cm⁻¹ could be

a P–O–H or a P–H stretch, indicating an interaction of phosphorus with H₂O on the surface of schreibersite.^{114,122,123,124} XPS analysis of the surface could help reveal which of the two types of phosphorus species are present since the P in P–O–H would be in a positive oxidation state (binding energy of 2p electron in P greater than about 130 eV), while the P in P–H would be in a negative oxidation state (binding energy less than about 130 eV).¹²⁵ Additionally, control experiments of H₂O dosed onto an FeNi sample at 295 K did not show this feature at 2400 cm⁻¹. Both the features at 3187 and 2423 cm⁻¹ suggest a strong chemical interaction between H₂O vapor and schreibersite. The shoulder at ~3400 cm⁻¹ and the relatively weak feature at 1680 cm⁻¹ are indicative of molecular H₂O bound to the surface (i.e., a hydrogen bonded O–H stretch and a H–O–H scissors motion, respectively).^{68,70} The difference in features observed for H₂O dosed at low temperature versus high temperature, in particular the appearance of peaks corresponding to dissociation of H₂O, suggests that the surface temperature of the mineral is an important aspect of its reactivity.

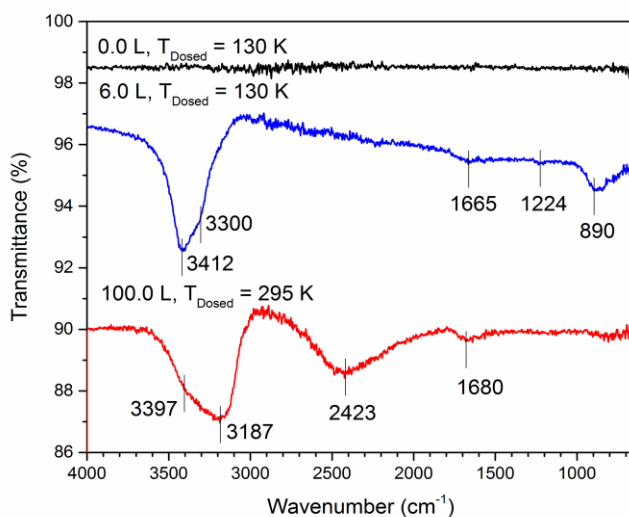


Figure 3.10 RAIRS spectra of H₂O dosed onto variable temperature surfaces of Fe₂NiP and FeNi (T_{Dosed} = surface temperature when H₂O was dosed). All spectra were acquired after cooling the sample to at least 130 K.

3.3 TPD Data and Analysis of Water (D_2O and H_2O)

The TPD spectra shown in Figure 3.11 provide further evidence of strong chemical interactions in addition to weaker intermolecular forces between schreibersite and H₂O. In this experiment, 6.0 Langmuirs of H₂O was dosed onto a 130 K Fe₂NiP surface and the temperature was increased with a ramp rate of 0.2 K/s. Low temperature peaks (i.e., 177 and 195 K) correspond to physisorption of molecular H₂O, while peaks at 503, 535 and 560 K are indicative of OH⁻ groups recombining to form H₂O and desorb after dissociative chemisorption on the surface. OH⁻ formation most likely happened during the TPD experiment. As the surface is heated, some of the H₂O on the surface dissociates into OH⁻, and these OH⁻ groups are more strongly bound to the surface than the original H₂O. As the surface temperature is further increased, the H₂O recombines

and desorbs. PO_x species are likely to form anions rather than cations and are not likely to be volatile under the conditions of these experiments, as compared to phosphate (PO_4^{3-}) desorption from an iron oxide surface.¹²⁶

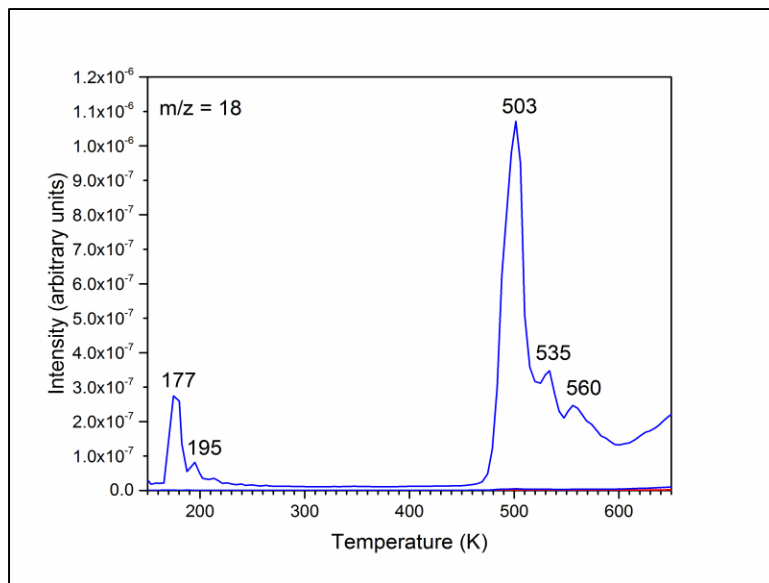


Figure 3.11 TPD spectrum of 6.0 L of H_2O dosed onto Fe_2NiP . A ramp rate of 0.2 K/s was used.

A challenging aspect of the TPD experiments was the difficulty of obtaining reproducible results. In particular, the chemisorption peaks shifted in temperature significantly between experiments, as observed by the comparison of Figure 3.11 to Figure 3.12. This shift is predicted to be a consequence of surface reconstruction due to different surface preparation procedures (e.g., flashing temperatures used during sputtering cycles).

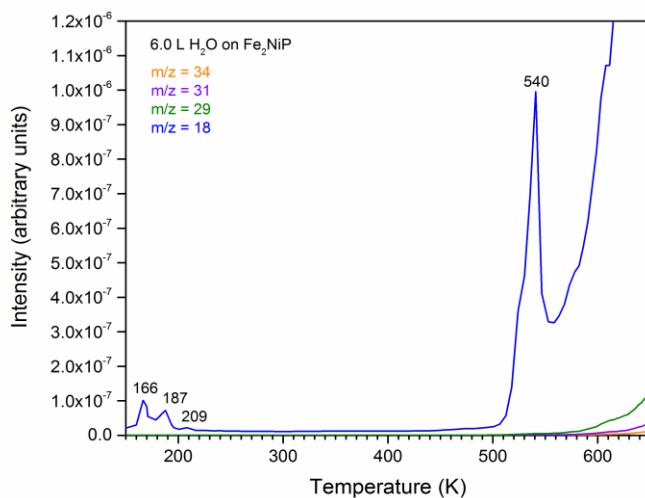


Figure 3.12 TPD spectrum of 6.0 L of H₂O dosed onto Fe₂NiP. A ramp rate of 0.2 K/s was used. Data was taken one day before the data illustrated in Figure 3.13.

In a separate TPD experiment, 5.0 L of H₂O and D₂O were compared to verify that the m/z = 18 detected by the QMS was H₂O dosed from the manifold. Figures 3.13 and 3.14 show the desorption of H₂O and D₂O after 5.0 L of each were dosed into the chamber, respectively. As expected, there is a shift in the TPD spectrum between the H₂O and D₂O experiments due to the difference in zero-point energies of the molecules.¹²⁷ The “bumps” at 164 and 166 K are indicative of the transition from the amorphous to crystalline phase.¹²⁷ These signatures of H₂O desorption suggest that the detection of m/z = 18 is representative of H₂O dosed from the manifold versus another species or background contamination. Unfortunately, the shape and temperature range of both chemisorption peaks have not been discovered in comparable model systems, and there are multiple sites at which the H₂O could desorb from (e.g. tungsten wires, tantalum

plate, iron plate around schreibersite, etc.), which consequently makes it difficult to determine the origin of these peaks.

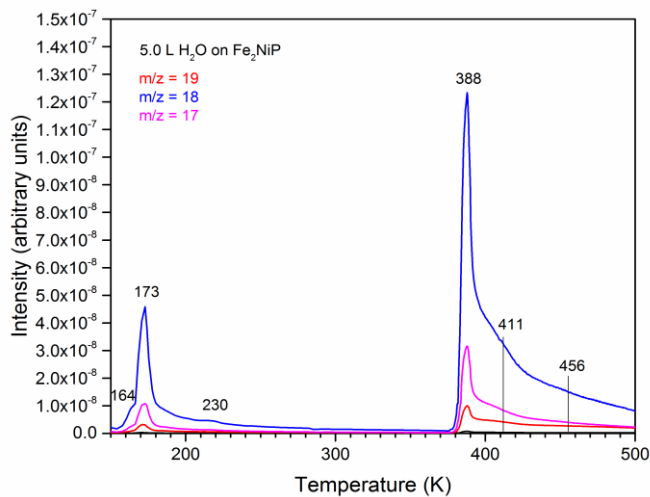


Figure 3.13 TPD spectrum of 5.0 L of H₂O dosed onto Fe₂NiP. A ramp rate of 0.2 K/s was used.

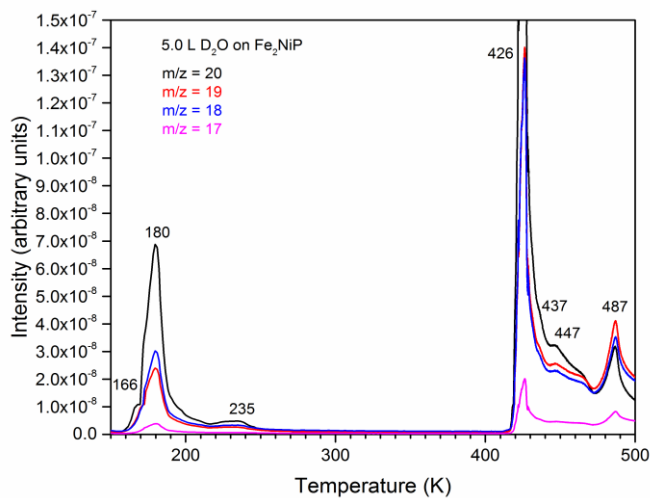


Figure 3.14 TPD spectrum of 5.0 L of D₂O dosed onto Fe₂NiP. A ramp rate of 0.2 K/s was used.

3.4 RAIRS Data and Analysis of H_2O_2

As mentioned previously, hydrogen peroxide 30 wt. % in H_2O was used, and therefore, it was hypothesized that the RAIRS spectra would appear similar to that of H_2O RAIRS spectra with the appearance of peaks representative of oxidation on the surface. Figure 3.15 illustrates RAIRS of H_2O_2 on a cold schreibersite surface. The peak that shifts to 857 cm^{-1} at a dosage of 8.0 L is indicative of the O–O stretch.⁷⁵ Transitions at $\sim 3400\text{ cm}^{-1}$ and 1663 cm^{-1} are very likely to indicate the O–H stretch and H–O–H bend of H_2O , respectively. The peak at 2478 cm^{-1} is unknown and could possibly represent oxidation on the surface. It is unexpected to not observe the 1220 cm^{-1} feature in this data. The disappearance of this band may indicate that the band is evidence of organic contamination rather than a P=O stretch.

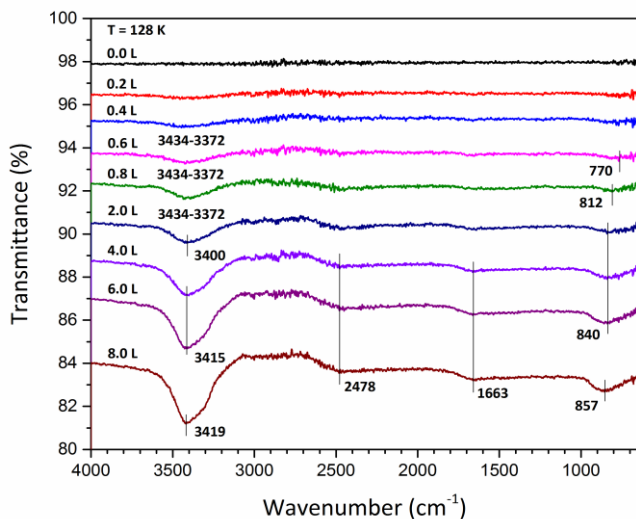


Figure 3.15 A RAIRS spectra of H_2O_2 adsorbed to Fe_2NiP with a H_2O_2 dosage of 0.2 L – 8.0 L. Experiments were run with a sample temperature of 128 K.

CHAPTER 4: SMALL ORGANICS ON SCHREIBERSITE

4.1 RAIRS Data and Analysis of CH₃OH on FeNi and Fe₂NiP

Similar to the analysis of the H₂O experiments, the adsorption of methanol (CH₃OH) on schreibersite was characterized by comparison of the vibrational bands in this experiment to band assignments in referenced experiments. The adsorption of CH₃OH on an FeNi sample was additionally performed to investigate the possible interaction of CH₃OH with lattice phosphorus atoms.

Figure 4.1 illustrates peaks that represent a Fe₂NiP surface exposed to varying dosages of CH₃OH. Similar to the analysis of H₂O adsorption, the frequencies observed in Figure 4.1 were assigned by comparison to RAIRS data of other model systems that are relevant to our experiments, e.g., thick ices and ices on nickel, iron, nickel oxide and iron oxide surfaces. This comparison is outlined in Table 4.1. Experimentally derived RAIRS frequencies and their relative intensities are: 1046–1040 cm⁻¹ (sharp), 3337–3230 cm⁻¹ (strong), 1462 cm⁻¹, 2836 cm⁻¹, 2957 cm⁻¹ (medium) and 1135 cm⁻¹, 1233 cm⁻¹ (weak). The band at 3337–3230 cm⁻¹ is assigned to the O–H stretch of CH₃OH in the condensed phase.¹²⁸ This band shifts as the dosage increases, and this shift is most likely attributed to dipole coupling and/or changes in the electronic environment at the interface. Comparing the experimental values to the referenced values in Table 4.1 makes

it difficult to ascertain whether CH₃OH is adsorbed to an iron/iron oxide or nickel/nickel oxide site.

At a dosage of 0.4 L (Figure 4.1), the only feature observable is the C–O stretch at 1040 cm⁻¹. The O–H stretch is clearly visible at 0.8 L, and the CH₃ deformation band (1462 cm⁻¹), symmetric stretch (2836 cm⁻¹) and asymmetric stretch (2957 cm⁻¹) do not appear until 4.0 L. Because the O–H stretch does not appear until 0.8 L, it is likely that below 0.8 L, CH₃OH dissociatively adsorbs to the surface and decomposes into methoxy (CH₃O⁻) and H⁺. This conclusion is supported by the fact that CH₃OH dissociation at low temperature has been observed on nickel surfaces.^{83,129} The suggested orientation of CH₃OH dissociation on the Fe₂NiP surface is depicted in Figure 4.2. Although it has been calculated that more energy is required to dissociate CH₃OH into CH₃O⁻ + H⁺ versus CH₃⁺ + OH⁻,¹³⁰ the appearance of the C–O stretch suggests that the O–H bond breaks upon contact with the surface. It is plausible that CO and H could be dissociation products, however, it would not be energetically favorable to break the C–H bonds.¹³¹ At 0.8 L, the appearance of the O–H stretch suggests the formation of CH₃OH multilayer ice. The vibrational modes of the CH groups are then also expected to appear at 0.8 L. However, it has been observed in other RAIRS experiments that these modes do not appear until higher dosages,^{128,132} and that is most likely due to the angle of the dipole moment with respect to the plane of the surface. At 4.0 L, all the peaks intrinsic to CH₃OH adsorption are observable in the data. Figure 4.3 shows the adsorption of CH₃OH on the surface of the FeNi control sample. Because the peak at ~1240 cm⁻¹ appears in the FeNi control experiment (Figure 4.3), it is difficult to make an argument that the band

represents the interaction of phosphorus with CH₃OH. In addition, comparison of the O–H stretching frequency in Figure 4.1 to Figure 4.3 shows that the frequency remained near 3300 cm⁻¹, which further supports the idea that CH₃OH does not interact with phosphorus at low surface temperatures.

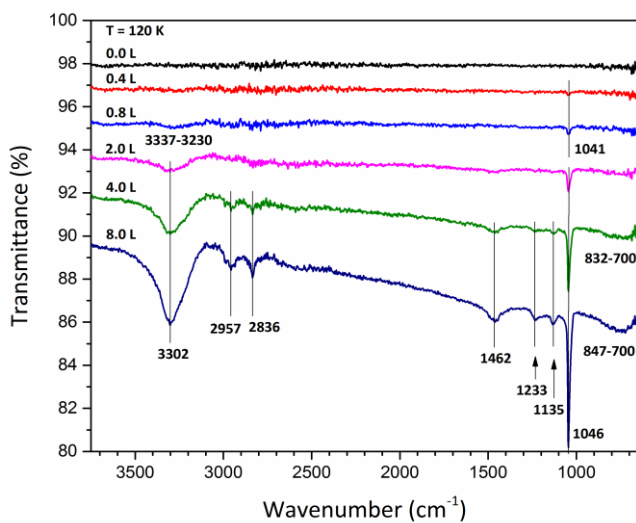


Figure 4.1 A RAIRS spectra of CH₃OH and CH₃OH dissociation products adsorbed to Fe₂NiP with a CH₃OH dosage of 0.4 L – 8.0 L Experiments were run with a sample temperature of 120 K.

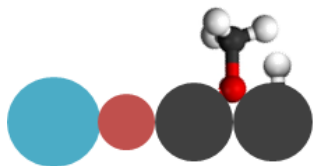


Figure 4.2 A drawing of the dissociation of CH₃OH as CH₃O⁻ and H⁺ on a cold Fe₂NiP surface.

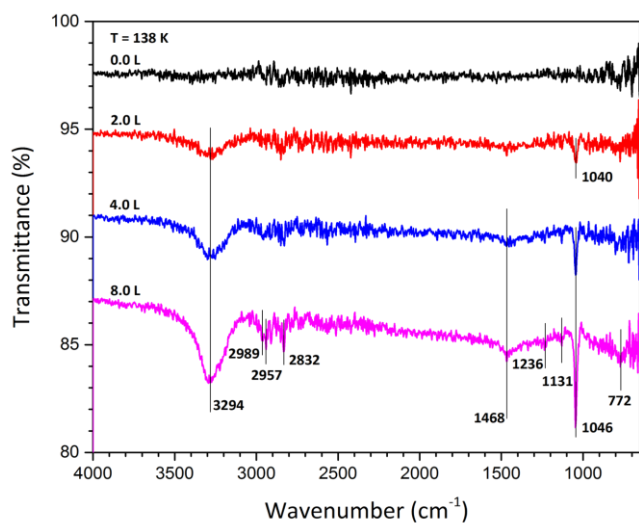


Figure 4.3 A RAIRS spectra of CH₃OH adsorbed to FeNi with a CH₃OH dosage of 2.0 L – 8.0 L Experiments were run with a sample temperature of 138 K.

Table 4.1

Vibrational frequencies (cm^{-1}) of CH_3OH adsorbed to Fe_2NiP at a CH_3OH dosage of 0.4 L – 8.0 L and a sample temperature of 120 K. Frequencies from other experiments are also shown.

dosage (L)	band assignment	this exp	other exp (iron/iron oxide substrate)	other exp (nickel/nickel oxide substrate)
0.4–8.0	OH bend	847–679	750–710 ^a	685, ^d 750 ^e
0.4–8.0	CO stretch	1046–1040	1050–1035 ^a	1035, ^d 1020 ^e
0.4–8.0	CH_3 rock	1135–1128		1155, ^d 1130 ^e
0.4–8.0	Unknown	1233		
0.4–8.0	CH_3 bend	1462	1480–1450, ^a 1440, ^b 1460 ^b	1480, ^c 1450 ^d
0.4–8.0	CH_3 symm stretch	2836	2850, ^a 2860 ^c	2810, ^d 2790 ^e
0.4 –8.0	CH_3 asymm stretch	2957	2950, ^a 2960 ^c	2920, ^d 2955 ^d 2950, ^c 2910 ^e
0.4–8.0	OH stretch	3337–3230	3300–3250, ^a 3460 ^b	3215, ^d 3210 ^e

^a Reference 78. ^b Reference 79. ^c Reference 80. ^d Reference 84. ^e Reference 82.

4.2 RAIRS Data and Analysis of HCO₂H

Figure 4.4 displays the adsorption of formic acid (HCO₂H) to the surface of the Fe₂NiP synthetic mineral. Compared to H₂O and CH₃OH, the adsorption of HCO₂H on model systems that are relevant to our experiments has not been well investigated. Therefore, the frequencies observed in Figure 4.5 were assigned by comparison to RAIRS data of ices on nickel and iron oxide terminated surfaces, as well as other metal surfaces such as copper and titanium dioxide. This comparison is outlined in Table 4.2. Experimentally derived RAIRS frequencies and their relative intensities are: 1733 cm⁻¹ (sharp), 2696 cm⁻¹ (broad), 972–959 cm⁻¹ (medium) and 1080 cm⁻¹, 1222 cm⁻¹ (weak). From the data and band assignments displayed in Figure 4.5 and Table 4.2, it is proposed that the adsorption geometry of HCO₂H on the schreibersite surface is that shown in Figure 4.4.

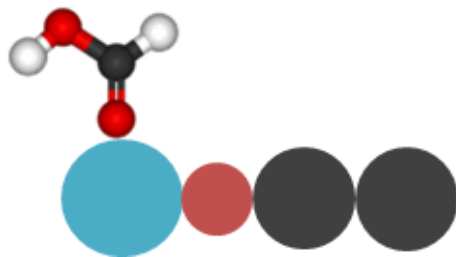


Figure 4.4 Suggested adsorption geometry of HCO₂H dosed on Fe₂NiP.

Several reasons support this hypothesis. Because the C–O–H bend at 972–959 cm⁻¹ is visible but the O–H stretching frequency is missing, it is likely that the geometry of the OH dipole moment is the cause of the attenuation of the OH band intensity. If this

is the case, then the C–H stretching frequency should also not be detected. The transition at $\sim 2700\text{ cm}^{-1}$ could plausibly represent the C–H stretch, however, the C–H stretch is commonly found in the higher frequency range of $\sim 2900\text{--}2800\text{ cm}^{-1}$.^{79,83,133,134} In addition, the spectra of HCO₂H adsorption on the FeNi sample shown in Figure 4.6 do not show a peak at $\sim 2700\text{ cm}^{-1}$, which suggests that the peak is related to an interaction with phosphorus. Deuterated formic acid experiments will be performed in the future to help clarify the band assignment. Other supporting evidence for the adsorption geometry proposed in Figure 4.4 would be the observation of a metal–oxide stretching frequency. Unfortunately, iron and nickel oxide stretching frequencies are below the detection limit of this experimental setup.

Unlike CH₃OH, it is proposed that HCO₂H remains in its molecular form upon contact with the surface. Due to the C=O stretching frequency at $\sim 1730\text{ cm}^{-1}$ and the lack of the strong C–H bending transition found among formate species,⁸³ HCO₂H presumably does not dissociate upon contact with the surface.

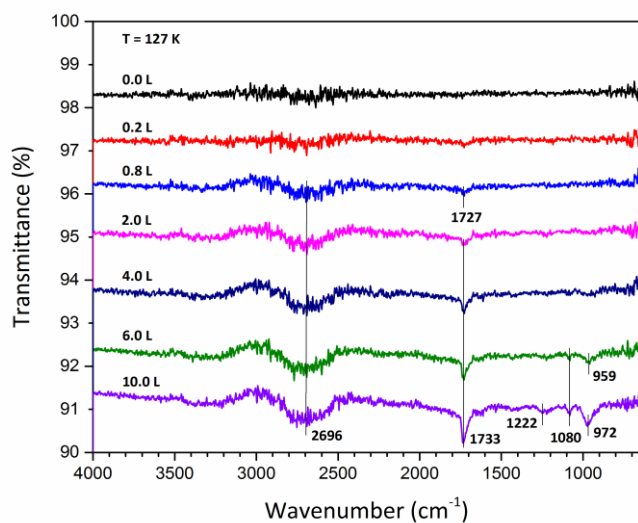


Figure 4.5 A RAIRS spectra of HCO₂H adsorbed to Fe₂NiP with a HCO₂H dosage of 0.2 L – 10.0 L Experiments were run with a sample temperature of 127 K.

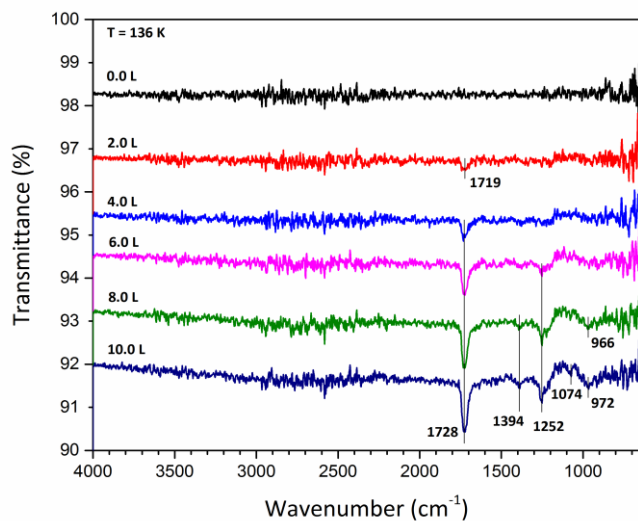


Figure 4.6 A RAIRS spectra of HCO₂H adsorbed to FeNi with a HCO₂H dosage of 2.0 L – 10.0 L Experiments were run with a sample temperature of 136 K.

Table 4.2

Vibrational frequencies (cm^{-1}) of HCO_2H adsorbed to Fe_2NiP at a HCO_2H dosage of 0.2 L – 8.0 L and a sample temperature of 127 K. Frequencies from other experiments are also shown.

dosage (L)	band assignment	this exp	other expts (various substrates)
0.2–8.0	C–O–H bend	972–959	960 ^a
0.2–8.0	CH out-of-plane bend	1080	1072 ^a
0.2–8.0	C–O stretch	1222	1240 ^a
	C=O stretch, multilayer	1733	1720, ^b 1715, ^c 1728 ^d
0.2–8.0	Unknown	2696	

^aReference 79. ^bReference 83. ^cReference 134. ^dReference 121.

^a = nickel substrate

^b = iron oxide substrate

^c = copper substrate

^d = titanium dioxide substrate

4.3 RAIRS Data for Molecular Probes

Pyridine ($\text{C}_5\text{H}_5\text{N}$), carbon monoxide (CO) and hydrogen (H_2) were exploited to probe the surface sites of schreibersite. Due to time, the $\text{C}_5\text{H}_5\text{N}$ data was not reproduced

and will not be used for the upcoming publication (Qasim and Abbott–Lyon, in prep.).

Figure 4.7 shows RAIRS spectra of Fe₂NiP exposed to various dosages of C₅H₅N.

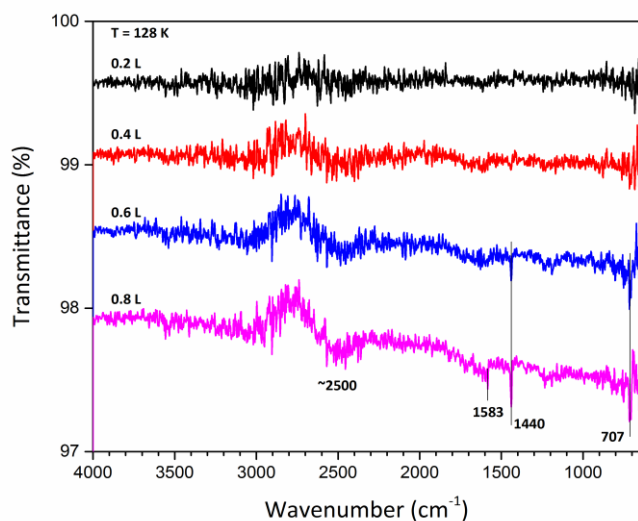


Figure 4.7 A RAIRS spectra of C₅H₅N adsorbed to Fe₂NiP with a C₅H₅N dosage of 0.2 L – 0.8 L. Experiments were run with a sample temperature of 128 K.

The peak at 1440 cm⁻¹ is representative of a weak Lewis acid site (or physisorption at the surface)¹³⁵ and the peak at 1583 cm⁻¹ features a weak Brønsted acid site.¹³⁶ The band at ~2500 cm⁻¹ may symbolize the protonation of C₅H₅N to the pyridinium ion. A plausible Brønsted acid source would be OH⁻ bound to the surface.

CO and H₂ were also dosed onto the schreibersite surface as probe molecules, but the peak intensities were either not observed or were so weak they could not clearly be assigned. The RAIRS spectra of CO dosed onto the Fe₂NiP surface shown in Figure 4.8 has two weak transitions at ~3000 cm⁻¹ and ~2400 cm⁻¹, which could represent background H₂O contamination and the oxidation of CO to CO₂, respectively. The

RAIRS spectra of H₂ dosed onto the Fe₂NiP surface shown in Figure 4.9 appears to not have any transitions.

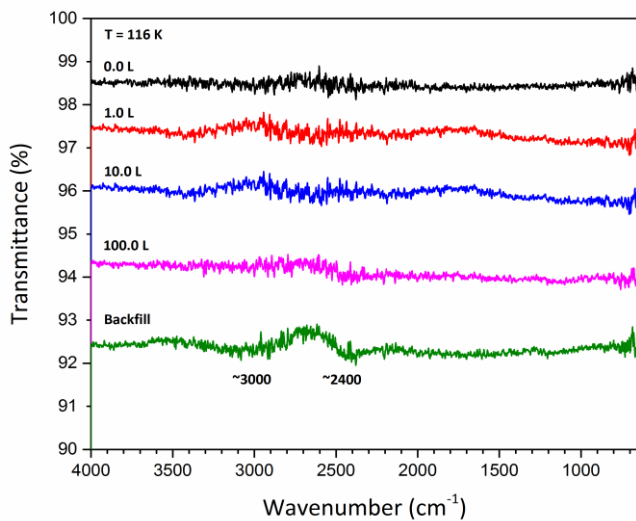


Figure 4.8 A RAIRS spectra of CO adsorbed to Fe₂NiP. Experiments were run with a sample temperature of 116 K.

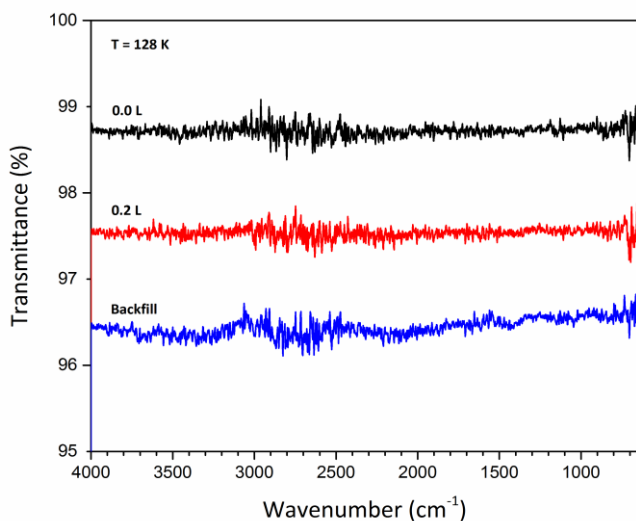


Figure 4.9 A RAIRS spectra of H₂ adsorbed to Fe₂NiP. Experiments were run with a sample temperature of 128 K.

CHAPTER 5: CONCLUSION

It is evident from this thesis that trying to understand the nature of the schreibersite surface is as complex as the surface itself and requires numerous experimental techniques. A custom-built UHV apparatus and the schreibersite sample were optimized in order to perform RAIRS and TPD experiments on the schreibersite surface. Before studying the ice–mineral interface, the surface was characterized by SEM/EDS and XPS. These studies provided the atomic composition at multiple sample depths, which suggested that phosphorus in schreibersite is reactive with H₂O vapor at standard temperature and pressure due to the higher abundance of phosphorus detected in the EDS data compared to the XPS data. An extensive RAIRS and TPD study was performed of H₂O adsorption on Fe₂NiP and FeNi and showed that the temperature of the surface influences surficial chemistry, the phosphorus in schreibersite is able to be oxidized under anoxic conditions in the presence of H₂O, and H₂O most likely interacts with lattice phosphorus at cold (< 130K) and high (~295 K) temperatures. H₂O₂ adsorption was studied to compare to the H₂O adsorption experiments, and it is possible that the peak at 2478 cm⁻¹ in the H₂O₂ data represents oxidation of the surface. The interaction of organic molecules, CH₃OH and HCO₂H, with the cold schreibersite surface was additionally studied. It was illustrated that CH₃O⁻ and H⁺ is formed on the surface at low CH₃OH dosages and most likely does not interact with lattice phosphorus. On the contrary, it is suggested that HCO₂H does not dissociate upon contact with the surface,

but could be interacting with phosphorus in the sample. No evidence of adsorption of either H₂ or CO on the Fe₂NiP surface was apparent by RAIRS. This could be due to surface selection rules or because the molecules are not able to stick to the surface under the conditions investigated in this work. Even at low dosages of C₅H₅N, Lewis and Brønsted acid sites were apparent in the RAIRS spectra, which is another piece of evidence that illustrates how chemically active the schreibersite surface is.

The next phase in the investigation of the schreibersite surface will include performing a flashing series to try to uncover the origin of the ~1220 cm⁻¹ peak, dosing deuterated HCO₂H to make an assignment of the ~2700 cm⁻¹ peak and constructing a new solid–liquid cell for polarization modulation (PM)–RAIRS experiments. The development of the liquid–solid cell will allow studies of the mineral surface–liquid interface *in-situ*, complementing the UHV studies and providing experimental conditions that parallel the aqueous–phase experiments performed by our collaborators in the Center for Chemical Evolution.

REFERENCES

1. Carenco, S.; Portehault, D.; Boissiere, C.; Mezailles, N.; Sanchez, C. Nanoscaled metal borides and phosphides: recent developments and perspectives. *Chem. Rev.* **2013**, *113*, 7981-8065.
2. Brock, S. L.; Perera, S. C.; Stamm, K. L. Chemical Routes for Production of Transition-Metal Phosphides on the Nanoscale: Implications for Advanced Magnetic and Catalytic Materials. *Chem. Eur. J.* **2004**, *10*, 3364-3371.
3. Zhang, H.; Ha, D.; Hovden, R.; Kourkoutis, L. F.; Robinson, R. D. Controlled synthesis of uniform cobalt phosphide hyperbranched nanocrystals using tri-n-octylphosphine oxide as a phosphorus source. *Nano Lett.* **2010**, *11*, 188-197.
4. Allen, G. C.; Carmalt, C. J.; Cowley, A. H.; Hector, A. L.; Kamepalli, S.; Lawson, Y. G.; Norman, N. C.; Parkin, I. P.; Pickard, L. K. Preparation and characterization of a material of composition BiP (bismuth phosphide) and other intergroup 15 element phases. *Chem. Mater.* **1997**, *9*, 1385-1392.
5. Shi, Y.; Zhang, B. Recent advances in transition metal phosphide nanomaterials: synthesis and applications in hydrogen evolution reaction. *Chem. Soc. Rev.* **2016**.
6. Kanatzidis, M. G.; Pöttgen, R.; Jeitschko, W. The metal flux: a preparative tool for the exploration of intermetallic compounds. *Angew. Chem. Int.* **2005**, *44*, 6996-7023.
7. Kloc, C.; Lux-Steiner, M. C.; Keil, M.; Baumann, J.; Doell, G.; Bucher, E. Growth and characterization of CuP₂ single crystals. *J. Cryst. Growth* **1990**, *106*, 635-642.
8. Odile, J.; Soled, S.; Castro, C.; Wold, A. Crystal growth and characterization of the transition-metal phosphides copper diphosphide, nickel diphosphide, and rhodium triphosphide. *Inorg. Chem.* **1978**, *17*, 283-286.
9. Payne, A. C.; Sprauve, A. E.; Holm, A. P.; Olmstead, M. M.; Kauzlarich, S. M.; Klavins, P. EuSnP: a novel antiferromagnet with two-dimensional, corrugated Sn sheets. *J. Alloys Compounds* **2002**, *338*, 229-234.
10. Reehuis, M.; Jeitschko, W.; Möller, M.; Brown, P. A Neutron diffraction study of the magnetic structure of EuCo₂P₂. *J. Phys. Chem. Solids* **1992**, *53*, 687-690.

11. Blanchard, P. E.; Grosvenor, A. P.; Cavell, R. G.; Mar, A. X-ray Photoelectron and Absorption Spectroscopy of Metal-Rich Phosphides M₂P and M₃P (M= Cr– Ni). *Chem. Mater.* **2008**, *20*, 7081-7088.
12. Zhao, H.; Oyama, S. T.; Freund, H.; Włodarczyk, R.; Sierka, M. Nature of active sites in Ni₂P hydrotreating catalysts as probed by iron substitution. *Appl. Catal. B-Environ.* **2015**, *164*, 204-216.
13. Layman, K. A.; Bussell, M. E. Infrared spectroscopic investigation of CO adsorption on silica-supported nickel phosphide catalysts. *J. Phys. Chem., B* **2004**, *108*, 10930-10941.
14. Cecilia, J.; Infantes-Molina, A.; Rodríguez-Castellón, E. Hydrodechlorination of polychlorinated molecules using transition metal phosphide catalysts. *J. Hazard. Mater.* **2015**, *296*, 112-119.
15. Zhou, L.; Kong, Y.; Du, Y.; Wang, J.; Zhou, Y. Spatial and electronic structure of the Ni₃P surface. *Appl. Surf. Sci.* **2010**, *256*, 7692-7695.
16. Oyama, S. T. Novel catalysts for advanced hydroprocessing: transition metal phosphides. *J. Catal.* **2003**, *216*, 343-352.
17. Zhao, H.; Li, D.; Bui, P.; Oyama, S. Hydrodeoxygenation of guaiacol as model compound for pyrolysis oil on transition metal phosphide hydroprocessing catalysts. *Appl. Catal., A* **2011**, *391*, 305-310.
18. Guan, Q.; Li, W. A novel synthetic approach to synthesizing bulk and supported metal phosphides. *J. Catal.* **2010**, *271*, 413-415.
19. Brock, S. L.; Senevirathne, K. Recent developments in synthetic approaches to transition metal phosphide nanoparticles for magnetic and catalytic applications. *J. Solid State Chem.* **2008**, *181*, 1552-1559.
20. Duan, X.; Huang, Y.; Cui, Y.; Wang, J.; Lieber, C. M. Indium phosphide nanowires as building blocks for nanoscale electronic and optoelectronic devices. *Nature* **2001**, *409*, 66-69.
21. Gillot, F.; Boyanov, S.; Dupont, L.; Doublet, M.; Morcrette, M.; Monconduit, L.; Tarascon, J. Electrochemical reactivity and design of NiP₂ negative electrodes for secondary Li-ion batteries. *Chem. Mater.* **2005**, *17*, 6327-6337.
22. Cabana, J.; Monconduit, L.; Larcher, D.; Palacin, M. R. Beyond Intercalation-Based Li-Ion Batteries: The State of the Art and Challenges of Electrode Materials Reacting Through Conversion Reactions. *Adv. Mater.* **2010**, *22*, E170-E192.

23. Tegus, O.; Brück, E.; Buschow, K.; De Boer, F. Transition-metal-based magnetic refrigerants for room-temperature applications. *Nature* **2002**, *415*, 150-152.
24. Barz, H.; Ku, H. C.; Meisner, G. P.; Fisk, Z.; Matthias, B. T. Ternary transition metal phosphides: High-temperature superconductors. *Proc. Natl. Acad. Sci. U. S. A.* **1980**, *77*, 3132-3134.
25. Wang, X.; Clark, P.; Oyama, S. T. Synthesis, characterization, and hydrotreating activity of several iron group transition metal phosphides. *J. Catal.* **2002**, *208*, 321-331.
26. Abu, I. I.; Smith, K. J. HDN and HDS of model compounds and light gas oil derived from Athabasca bitumen using supported metal phosphide catalysts. *Appl. Catal., A. Gen.* **2007**, *328*, 58-67.
27. Oyama, S. T.; Gott, T.; Zhao, H.; Lee, Y. Transition metal phosphide hydroprocessing catalysts: a review. *Catal. Today.* **2009**, *143*, 94-107.
28. Prins, R.; Bussell, M. E. Metal phosphides: preparation, characterization and catalytic reactivity. *Catal. Lett.* **2012**, *142*, 1413-1436.
29. Zhao, H.; Li, D.; Bui, P.; Oyama, S. Hydrodeoxygenation of guaiacol as model compound for pyrolysis oil on transition metal phosphide hydroprocessing catalysts. *Appl. Catal., A. Gen.* **2011**, *391*, 305-310.
30. Bui, P.; Cecilia, J. A.; Oyama, S. T.; Takagaki, A.; Infantes-Molina, A.; Zhao, H.; Li, D.; Rodríguez-Castellón, E.; López, A. J. Studies of the synthesis of transition metal phosphides and their activity in the hydrodeoxygenation of a biofuel model compound. *J. Catal.* **2012**, *294*, 184-198.
31. Chen, J.; Ci, D.; Wang, R.; Zhang, J. Hydrodechlorination of chlorobenzene over NiB/SiO₂ and NiP/SiO₂ amorphous catalysts after being partially crystallized: A consideration of electronic and geometrical factors. *Appl. Surf. Sci.* **2008**, *255*, 3300-3309.
32. Chen, J.; Sun, L.; Wang, R.; Zhang, J. Hydrodechlorination of chlorobenzene over Ni₂P/SiO₂ catalysts: influence of Ni₂P loading. *Catal. Lett.* **2009**, *133*, 346-353.
33. Liu, X.; Chen, J.; Zhang, J. Hydrodechlorination of chlorobenzene over silica-supported nickel phosphide catalysts. *Ind Eng Chem Res* **2008**, *47*, 5362-5368.
34. Feng, L.; Vrubel, H.; Bensimon, M.; Hu, X. Easily-prepared dinickel phosphide (Ni₂P) nanoparticles as an efficient and robust electrocatalyst for hydrogen evolution. *Phys. Chem. Chem. Phys.* **2014**, *16*, 5917-5921.

35. Huang, Z.; Chen, Z.; Chen, Z.; Lv, C.; Meng, H.; Zhang, C. Ni₁₂P₅ Nanoparticles as an Efficient Catalyst for Hydrogen Generation via Electrolysis and Photoelectrolysis. *ACS nano* **2014**, *8*, 8121-8129.
36. Popczun, E. J.; McKone, J. R.; Read, C. G.; Biacchi, A. J.; Wiltrout, A. M.; Lewis, N. S.; Schaak, R. E. Nanostructured nickel phosphide as an electrocatalyst for the hydrogen evolution reaction. *J. Am. Chem. Soc.* **2013**, *135*, 9267-9270.
37. Popczun, E. J.; Roske, C. W.; Read, C. G.; Crompton, J. C.; McEnaney, J. M.; Callejas, J. F.; Lewis, N. S.; Schaak, R. E. Highly branched cobalt phosphide nanostructures for hydrogen-evolution electrocatalysis. *J. Mater. Chem., A* **2015**, *3*, 5420-5425.
38. Horton, H. R.; Moran, L. A.; Ochs, R. S.; Rawn, J. D.; Scrimgeour, K. G. *Principles of biochemistry*; Prentice Hall Upper Saddle River: 1996; .
39. Gulick, A. Phosphorus as a factor in the origin of life. *Am. Sci.* **1955**, 479-489.
40. Pasek, M. A.; Lauretta, D. S. Aqueous corrosion of phosphide minerals from iron meteorites: a highly reactive source of prebiotic phosphorus on the surface of the early Earth. *Astrobiology* **2005**, *5*, 515-535.
41. Pasek, M. Role of Phosphorus in Prebiotic Chemistry. *Astrobiology: An Evolutionary Approach* **2014**, 257.
42. Pasek, M. A.; Dworkin, J. P.; Lauretta, D. S. A radical pathway for organic phosphorylation during schreibersite corrosion with implications for the origin of life. *Geochim. Cosmochim. Acta* **2007**, *71*, 1721-1736.
43. Pasek, M. A.; Kee, T. P.; Bryant, D. E.; Pavlov, A. A.; Lunine, J. I. Production of potentially prebiotic condensed phosphates by phosphorus redox chemistry. *Angew. Chem. Int.* **2008**, *47*, 7918-7920.
44. Pasek, M. A.; Kee, T. P. In *On the origin of phosphorylated biomolecules*; Origins of Life: The Primal Self-Organization; Springer: 2011; pp 57-84.
45. Pirim, C.; Pasek, M.; Sokolov, D.; Sidorov, A.; Gann, R.; Orlando, T. Investigation of schreibersite and intrinsic oxidation products from Sikhote-Alin, Seymchan, and Odessa meteorites and Fe₃P and Fe₂NiP synthetic surrogates. *Geochim. Cosmochim. Acta* **2014**, *140*, 259-274.
46. Bryant, D. E.; Kee, T. P. Direct evidence for the availability of reactive, water soluble phosphorus on the early Earth. H-Phosphinic acid from the Nantan meteorite. *Chem. Commun.* **2006**, 2344-2346.

47. Pasek, M. A. Rethinking early Earth phosphorus geochemistry. *Proc. Natl. Acad. Sci. U. S. A.* **2008**, *105*, 853-858.
48. Pasek, M. A.; Harnmeijer, J. P.; Buick, R.; Gull, M.; Atlas, Z. Evidence for reactive reduced phosphorus species in the early Archean ocean. *Proc. Natl. Acad. Sci. U. S. A.* **2013**, *110*, 10089-10094.
49. Gull, M.; Mojica, M. A.; Fernandez, F. M.; Gaul, D. A.; Orlando, T. M.; Liotta, C. L.; Pasek, M. A. Nucleoside phosphorylation by the mineral schreibersite. *Sci. Rep.* **2015**, *5*, 17198.
50. Anthony, J.; Bideaux, R.; Bladh, K.; Nichols, M. *Handbook of Mineralogy. Chantilly, VA 20151-1110, USA. Mineralogical Society of America, Version 1.2001-2205* .
51. Skála, R.; Císarová, I. In *In Crystal structure of schreibersite from the meteoritic iron Sikhote Alin*; Lunar and Planetary Institute Science Conference Abstracts; 2001; Vol. 32, pp 1564.
52. Skála, R.; Drábek, M. Powder data for synthetic analogue of a mineral nickelphosphide. *Powder Diffr.* **2002**, *17*, 322-325.
53. Bryant, D. E.; Greenfield, D.; Walshaw, R. D.; Johnson, B. R.; Herschy, B.; Smith, C.; Pasek, M. A.; Telford, R.; Scowen, I.; Munshi, T. Hydrothermal modification of the Sikhote-Alin iron meteorite under low pH geothermal environments. A plausibly prebiotic route to activated phosphorus on the early Earth. *Geochim. Cosmochim. Acta* **2013**, *109*, 90-112.
54. Pasek, M.; Lauretta, D. Extraterrestrial flux of potentially prebiotic C, N, and P to the early Earth. *Origins of Life and Evolution of Biospheres* **2008**, *38*, 5-21.
55. Kolasinski, K. W. *Surface science: foundations of catalysis and nanoscience*; John Wiley & Sons: 2012; .
56. Houston, P. L. *Chemical kinetics and reaction dynamics*; Courier Corporation: 2012; .
57. Hazen, R. M. Chiral crystal faces of common rock-forming minerals. *Progress in Biological Chirality* **2004**, 137-151.
58. Hazen, R. M.; Sverjensky, D. A. Mineral surfaces, geochemical complexities, and the origins of life. *Cold Spring Harb Perspect. Biol.* **2010**, *2*, a002162.
59. Lasaga, A. Atomic treatment of mineral-water surface reactions. *Rev. Mineral. Geochem.* **1990**, *23*, 17-85.

60. De Yoreo, J. J.; Dove, P. M. Shaping crystals with biomolecules. *Science* **2004**, *306*, 1301-1302.
61. Hazen, R. M.; Sholl, D. S. Chiral selection on inorganic crystalline surfaces. *Nat. Mater.* **2003**, *2*, 367-374.
62. Orme, C.; Noy, A.; Wierzbicki, A.; McBride, M.; Grantham, M.; Teng, H.; Dove, P.; DeYoreo, J. Formation of chiral morphologies through selective binding of amino acids to calcite surface steps. *Nature* **2001**, *411*, 775-779.
63. Teng, H. H.; Dove, P. M. Surface site-specific interactions of aspartate with calcite during dissolution: Implications for biomineralization. *Am. Mineral.* **1997**, *82*, 878-887.
64. Brady, P. V. *The Physics and Chemistry of Mineral Surfaces*; CRC Press: 1996; .
65. Vlemmings, W. H.; Diamond, P. J.; Imai, H. A magnetically collimated jet from an evolved star. *Nature* **2006**, *440*, 58-60.
66. Fraser, H. J.; Collings, M. P.; McCoustra, M. R.; Williams, D. A. Thermal desorption of water ice in the interstellar medium. *Mon. Not. R. Astron. Soc.* **2001**, *327*, 1165-1172.
67. Eisner, J. A. Water vapour and hydrogen in the terrestrial-planet-forming region of a protoplanetary disk. *Nature* **2007**, *447*, 562-564.
68. Hock, M.; Seip, U.; Bassignana, I.; Wagemann, K.; Küppers, J. Coadsorption of oxygen and water at Ni (110) surfaces. *Surf. Sci. Lett.* **1986**, *177*, L978-L982.
69. Hung, W.; Schwartz, J.; Bernasek, S. Adsorption of H₂O on oxidized Fe (100) surfaces: comparison between the oxidation of iron by H₂O and O₂. *Surf. Sci.* **1993**, *294*, 21-32.
70. Hung, W.; Schwartz, J.; Bernasek, S. L. Sequential oxidation of Fe (100) by water adsorption: formation of an ordered hydroxylated surface. *Surf. Sci.* **1991**, *248*, 332-342.
71. Olle, L.; Salmeron, M.; Baro, A. The adsorption and decomposition of water on Ni (110) studied by electron energy loss spectroscopy. *J. Vac. Sci. Technol., A* **1985**, *3*, 1866-1870.
72. Baro, A.; Erley, W. The adsorption of H₂O on Fe (100) studied by EELS. *J. Vac. Sci. Technol.* **1982**, *20*, 580-583.

73. Frederick, B.; Jones, T.; Pudney, P.; Richardson, N. HREELS and RAIRS? A complete vibrational study of the surface benzoate species adsorbed on copper. *J. Electron. Spectrosc. Relat. Phenom.* **1993**, *64*, 115-122.
74. Borda, M. J.; Elsetinow, A. R.; Schoonen, M. A.; Strongin, D. R. Pyrite-induced hydrogen peroxide formation as a driving force in the evolution of photosynthetic organisms on an early Earth. *Astrobiology* **2001**, *1*, 283-288.
75. Lin, W.; Frei, H. Photochemical and FT-IR probing of the active site of hydrogen peroxide in Ti silicalite sieve. *J. Am. Chem. Soc.* **2002**, *124*, 9292-9298.
76. Almeida, G. C.; Andrade, D. P.; Arantes, C.; Nazareth, A. M.; Boechat-Roberty, H. M.; Rocco, M. L. M. Desorption from Methanol and Ethanol Ices by High Energy Electrons: Relevance to Astrochemical Models. *J. Phys. Chem., C* **2012**, *116*, 25388-25394.
77. Schlesinger, G.; Miller, S. L. Prebiotic synthesis in atmospheres containing CH₄, CO, and CO₂. *J. Mol. Evol.* **1983**, *19*, 376-382.
78. McBreen, P.; Erley, W.; Ibach, H. The adsorption and decomposition of methanol on Fe (110). *Surf. Sci.* **1983**, *133*, L469-L474.
79. Busca, G.; Lorenzelli, V. Infrared study of methanol, formaldehyde, and formic acid adsorbed on hematite. *J. Catal.* **1980**, *66*, 155-161.
80. Blyholder, G.; Neff, L. D. Infrared study of the adsorption of methanol, ethanol, ether, and water and the interaction of carbon monoxide and hydrogen on a nickel surface. *J. Catal.* **1963**, *2*, 138-144.
81. Wu, M. C.; Truong, C. M.; Goodman, D. W. Interactions of alcohols with a nickel oxide (100) surface studied by high-resolution electron energy loss spectroscopy and temperature-programmed desorption spectroscopy. *J. Phys. Chem.* **1993**, *97*, 9425-9433.
82. Bare, S. R.; Stroscio, J. A.; Ho, W. Characterization of the Adsorption and Decomposition of Methanol on Ni (110). *Surf. Sci.* **1985**, *150*, 399-418.
83. Haq, S.; Love, J.; Sanders, H.; King, D. Adsorption and decomposition of formic acid on Ni {110}. *Surf. Sci.* **1995**, *325*, 230-242.
84. Wu, M. C.; Truong, C. M.; Goodman, D. W. Interactions of alcohols with a nickel oxide (100) surface studied by high-resolution electron energy loss spectroscopy and temperature-programmed desorption spectroscopy. *J. Phys. Chem.* **1993**, *97*, 9425-9433.

85. Smith, K. E.; Callahan, M. P.; Gerakines, P. A.; Dworkin, J. P.; House, C. H. Investigation of pyridine carboxylic acids in CM2 carbonaceous chondrites: Potential precursor molecules for ancient coenzymes. *Geochim. Cosmochim. Acta* **2014**, *136*, 1-12.
86. Barzetti, T.; Selli, E.; Moscotti, D.; Forni, L. Pyridine and ammonia as probes for FTIR analysis of solid acid catalysts. *J. Chem. Soc., Faraday Trans.* **1996**, *92*, 1401-1407.
87. Duan, X.; Teng, Y.; Wang, A.; Kogan, V. M.; Li, X.; Wang, Y. Role of sulfur in hydrotreating catalysis over nickel phosphide. *J. Catal.* **2009**, *261*, 232-240.
88. Lee, Y.; Oyama, S. T. Bifunctional nature of a SiO₂-supported Ni₂P catalyst for hydrotreating: EXAFS and FTIR studies. *J. Catal.* **2006**, *239*, 376-389.
89. Parfitt, R. L.; Russell, J. D.; Farmer, V. C. Confirmation of the surface structures of goethite (α -FeOOH) and phosphated goethite by infrared spectroscopy. *J. Chem. Soc. Faraday Trans.: Physical Chemistry in Condensed Phases* **1976**, *72*, 1082-1087.
90. Rochester, C. H.; Topham, S. A. Infrared studies of the adsorption of probe molecules onto the surface of goethite. *J. Chem. Soc. Faraday Trans.: Physical Chemistry in Condensed Phases* **1979**, *75*, 872-882.
91. Rochester, C. H.; Topham, S. A. Infrared studies of the adsorption of probe molecules onto the surface of haematite. *J. Chem. Soc. Faraday Trans.: Physical Chemistry in Condensed Phases* **1979**, *75*, 1259-1267.
92. Leclerc, H.; Vimont, A.; Lavalley, J.; Daturi, M.; Wiersum, A. D.; Llwellyn, P. L.; Horcajada, P.; Férey, G.; Serre, C. Infrared study of the influence of reducible iron (iii) metal sites on the adsorption of CO, CO₂, propane, propene and propyne in the mesoporous metal-organic framework MIL-100. *Phys. Chem. Chem. Phys.* **2011**, *13*, 11748-11756.
93. Burke, D. J.; Puletti, F.; Brown, W. A.; Woods, P. M.; Viti, S.; Slater, B. Glycolaldehyde, methyl formate and acetic acid adsorption and thermal desorption from interstellar ices. *Mon. Not. R. Astron. Soc.* **2015**, *447*, 1444-1451.
94. Pradier, C.; Chabal, Y. J. *Biointerface characterization by advanced IR spectroscopy*; Elsevier: 2011; .
95. Yates Jr, J. T.; Madey, T. E. *Vibrational spectroscopy of molecules on surfaces.* **1987**.
96. Brundle, C.; Morawitz, H. *Vibrations at Surfaces*; Elsevier: 1983; .

97. Mizuse, K. *Spectroscopic Investigations of Hydrogen Bond Network Structures in Water Clusters*; Springer Science & Business Media: 2013; .
98. Wandelt, K. *Surface and Interface Science, Volumes 1 and 2: Volume 1-Concepts and Methods; Volume 2-Properties of Elemental Surfaces*; John Wiley & Sons: 2012; Vol. 1.
99. Hoffmann, F. M. Infrared reflection-absorption spectroscopy of adsorbed molecules. *Surf. Sci. Rep.* **1983**, 3, 107-192.
100. Miessler, G.; Tarr, D. *Inorganic Chemistry Pearson Prentice Hall*. Upper Saddle Rive, NJ **2004**.
101. Zecchina, A.; Scarano, D.; Reller, A. Infrared spectra of CO adsorbed on prismatic faces of α -Fe₂O₃. *J. Chem. Soc. Faraday Trans.: Physical Chemistry in Condensed Phases* **1988**, 84, 2327-2333.
102. Masel, R. I. *Principles of adsorption and reaction on solid surfaces*; John Wiley & Sons: 1996; Vol. 3.
103. Roberts, M. W.; McKee, C. *Chemistry of the metal-gas interface*; Oxford University Press, USA: 1978; .
104. Goldstein, J. I.; Newbury, D. E.; Echlin, P.; Joy, D. C.; Fiori, C.; Lifshin, E. *Scanning electron microscopy and X-ray microanalysis. A text for biologists, materials scientists, and geologists*. Plenum Publishing Corporation: 1981; .
105. Newbury, D. E.; Ritchie, N. W. Elemental mapping of microstructures by scanning electron microscopy-energy dispersive X-ray spectrometry (SEM-EDS): extraordinary advances with the silicon drift detector (SDD). *J. Anal. At. Spectrom.* **2013**, 28, 973-988.
106. Smentkowski, V. S. *Surface Analysis and Techniques in Biology*; Springer: 2014; .
107. Batley, G. E. *Trace Element Speciation Analytical Methods and Problems*; CRC Press: 1989; .
108. Boda, G.; Stenström, B.; Sagredo, V.; Beckman, O.; Carlsson, B.; Rundqvist, S. Magnetic and electric properties of FeP₂ single crystals. *Phys. Scripta* **1971**, 4, 132.
109. Hulliger, F. Electrical Properties of Pyrite-Type and Related Compounds with Zero Spin Moment. *Nature* **1963**, 200, 1064-1065.
110. Sharon, M.; Tamizhmani, G. Transition metal phosphide semiconductors for their possible use in photoelectrochemical cells and solar chargeable battery (Saur Vidyut Kosh V). *J. Mater. Sci.* **1986**, 21, 2193-2201.

111. La Cruz, N. L. *Schreibersite: Synthesis, Characterization and Corrosion and Possible Implications for Origin of Life*. **2015**.
112. Wieckowski, A.; Korzeniewski, C.; Braunschweig, B. *Vibrational Spectroscopy at Electrified Interfaces*; John Wiley & Sons: 2013; Vol. 10.
113. Bolina, A. S.; Wolff, A. J.; Brown, W. A. Reflection absorption infrared spectroscopy and temperature-programmed desorption studies of the adsorption and desorption of amorphous and crystalline water on a graphite surface. *J. Phys. Chem., B* **2005**, *109*, 16836-16845.
114. Carter, R.; Gierczak, C.; Dickie, R. The chemical interaction of organic materials with metal substrates. Part II: FT-IR studies of organic phosphate films on steel. *Appl. Spectrosc.* **1986**, *40*, 649-655.
115. Frey, B. L.; Hanken, D. G.; Corn, R. M. Vibrational spectroscopic studies of the attachment chemistry for zirconium phosphonate multilayers at gold and germanium surfaces. *Langmuir* **1993**, *9*, 1815-1820.
116. Hunt, R. D.; Mitchell, M. L.; Dluhy, R. A. The interfacial structure of phospholipid monolayer films: an infrared reflectance study. *J. Mol. Struct.* **1989**, *214*, 93-109.
117. Mendelsohn, R.; Brauner, J. W.; Gericke, A. External infrared reflection absorption spectrometry of monolayer films at the air-water interface. *Annu. Rev. Phys. Chem.* **1995**, *46*, 305-334.
118. Kanan, S. M.; Tripp, C. P. An infrared study of adsorbed organophosphonates on silica: a prefiltering strategy for the detection of nerve agents on metal oxide sensors. *Langmuir* **2001**, *17*, 2213-2218.
119. Schwaner, A.; Fieberg, J. E.; White, J. Methyl formate on Ag (111). 1. Thermal adsorption-desorption characteristics and alignment in monolayers. *J. Phys. Chem., B* **1997**, *101*, 11112-11118.
120. Turner, A. M.; Abplanalp, M. J.; Chen, S. Y.; Chen, Y. T.; Chang, A. H.; Kaiser, R. I. A photoionization mass spectroscopic study on the formation of phosphanes in low temperature phosphine ices. *Phys. Chem. Chem. Phys.* **2015**, *17*, 27281-27291.
121. Connor, P.; McQuillan, A. J. Phosphate adsorption onto TiO₂ from aqueous solutions: an in situ internal reflection infrared spectroscopic study. *Langmuir* **1999**, *15*, 2916-2921.
122. Dayanand, C.; Bhikshamaiah, G.; Tyagaraju, V. J.; Salagram, M.; Murthy, A. K. Structural investigations of phosphate glasses: a detailed infrared study of the x (PbO)-(1-x) P₂O₅ vitreous system. *J. Mater. Sci.* **1996**, *31*, 1945-1967.

123. Koutsopoulos, S. Synthesis and characterization of hydroxyapatite crystals: a review study on the analytical methods. *J. Biomed. Mater. Res.* **2002**, *62*, 600-612.
124. Berry, E.; Baddiel, C. Some assignments in the infra-red spectrum of octacalcium phosphate. *Spectrochim. Acta, Pt. A: Mol. Spectrosc.* **1967**, *23*, 1781-1792.
125. Pelavin, M.; Hendrickson, D.; Hollander, J.; Jolly, W. Phosphorus 2p electron binding energies. Correlation with extended Hueckel charges. *J. Phys. Chem.* **1970**, *74*, 1116-1121.
126. Nooney, M.; Campbell, A.; Murrell, T.; Lin, X.; Hossner, L.; Chusuei, C. C.; Goodman, D. Nucleation and growth of phosphate on metal oxide thin films. *Langmuir* **1998**, *14*, 2750-2755.
127. Smith, R. S.; Matthiesen, J.; Knox, J.; Kay, B. D. Crystallization Kinetics and Excess Free Energy of H₂O and D₂O Nanoscale Films of Amorphous Solid Water. *J. Phys. Chem., A* **2011**, *115*, 5908-5917.
128. Bolina, A.; Wolff, A.; Brown, W. Reflection absorption infrared spectroscopy and temperature programmed desorption investigations of the interaction of methanol with a graphite surface. *J. Chem. Phys.* **2005**, *122*, 044713-044711.
129. Miragliotta, J.; Polizzotti, R.; Rabinowitz, P.; Cameron, S.; Hall, R. IR-visible sum-frequency generation study of methanol adsorption and reaction on Ni (100). *Chem. Phys.* **1990**, *143*, 123-130.
130. Bauschlicher Jr, C. W.; Langhoff, S. R.; Walch, S. P. Theoretical study of the bond dissociation energies of methanol. *J. Chem. Phys.* **1992**, *96*, 450-454.
131. Shustorovich, E.; Sellers, H. The UBI-QEP method: a practical theoretical approach to understanding chemistry on transition metal surfaces. *Surf. Sci. Rep.* **1998**, *31*, 1-119.
132. Barros, R. B.; Garcia, A. R.; Ilharco, L. M. The decomposition pathways of methanol on clean Ru (0001), studied by reflection-absorption infrared spectroscopy (RAIRS). *J. Phys. Chem., B* **2001**, *105*, 11186-11193.
133. Popova, G. Y.; Andrushkevich, T.; Chesalov, Y. A.; Stoyanov, E. In situ FTIR study of the adsorption of formaldehyde, formic acid, and methyl formate at the surface of TiO₂ (anatase). *Kinet. Catal.* **2000**, *41*, 805-811.
134. Hayden, B.; Prince, K.; Woodruff, D.; Bradshaw, A. An IRAS study of formic acid and surface formate adsorbed on Cu (110). *Surf. Sci.* **1983**, *133*, 589-604.
135. Froment, G.; Delmon, B.; Grange, P. Hydrotreatment and hydrocracking of oil fractions. *Stud. Surf. Sci. Catal., (Feb.17, 1997)* **1997**.

136. Akçay, M. The surface acidity and characterization of Fe-montmorillonite probed by in situ FT-IR spectroscopy of adsorbed pyridine. *Appl. Catal., A. Gen.* **2005**, *294*, 156-160.
137. Roberts, M. W.; McKee, C. *Chemistry of the metal-gas interface*; Oxford University Press, USA: 1978; .